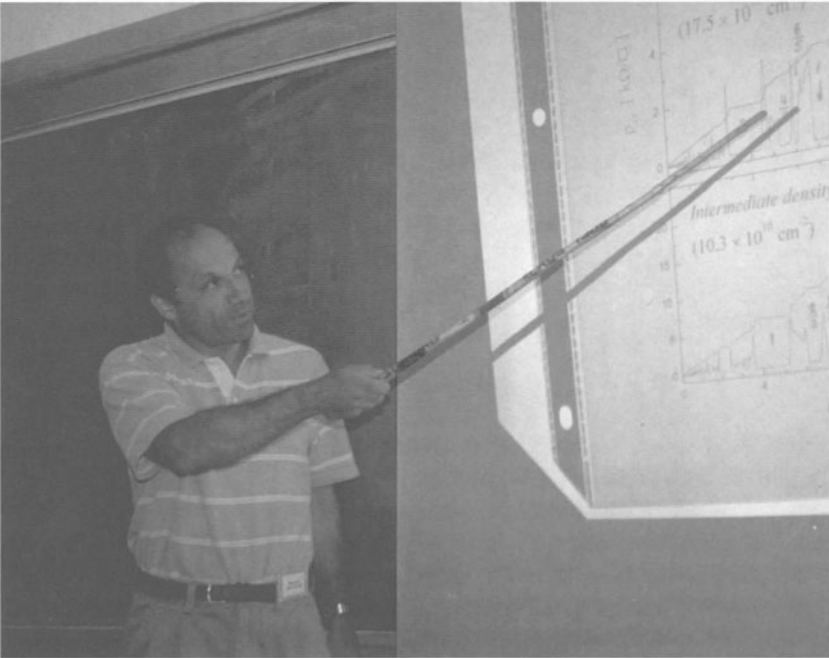COURSE 1

ELECTRONS IN A FLATLAND

M. SHAYEGAN

*Department of Electrical Engineering,
Princeton University, Princeton,
New Jersey, U.S.A.*

Contents

ELECTRONS IN A FLATLAND

M. Shayegan

1 Introduction

Electrons in a "flatland" are amazing! A simple low-temperature measurement of the resistance of a two-dimensional electron system (2DES) as a function of perpendicular magnetic field (B) reveals why (Fig. 1). In this figure the resistivities along (ρ_{xx}) and perpendicular (ρ_{xy}) to the direction of current are shown, and the vertical markings denote the Landau-level filling factor (ν). Look how the behavior of ρ_{xx} with temperature (T), shown schematically in the inset, changes as a function of the magnetic field. At certain fields, marked **A**, ρ_{xx} drops exponentially with decreasing temperature and approaches zero as $T \to 0$. This is the quantum Hall effect (QHE) and, as you can see in the other trace of Figure 1, the Hall resistance (ρ_{xy}) becomes quantized near these fields. The QHE is best described as an incompressible quantum liquid which often possesses a high degree of short-range electron correlation. Next, look at the T-dependence of ρ_{xx} at the fields marked **B** (near 13 and 14 T for this sample). Here ρ_{xx} exponentially *increases* with decreasing T, signaling an insulating behavior. The nature of this insulating state is not entirely clear, but it is generally believed that it is a pinned Wigner solid, a "crystal" of electrons with long-range positional order. Now look at what happens at the magnetic field marked **C**. At this field, ρ_{xx} shows a nearly temperature-independent behavior, reminiscent of a metal. It turns out that at this particular field there are two flux quanta per each electron. The electron magically combines with the two flux quanta and forms the celebrated "composite Fermion", a quasiparticle which now moves around in the 2D plane as if no external magnetic field was applied.

So in one sweep, just changing the magnetic field, the 2DES shows a variety of ground states ranging from insulating to metallic to "superconducting-like". And, as it turns out, these ground states are stabilized primarily by strong electron-electron correlations. The data of Figure 1 reveals the extreme richness of this system, one which has rendered the field of 2D carrier systems in a high magnetic field among the most active and exciting in solid state physics. It has already led to two physics Nobel prizes, one in 1985
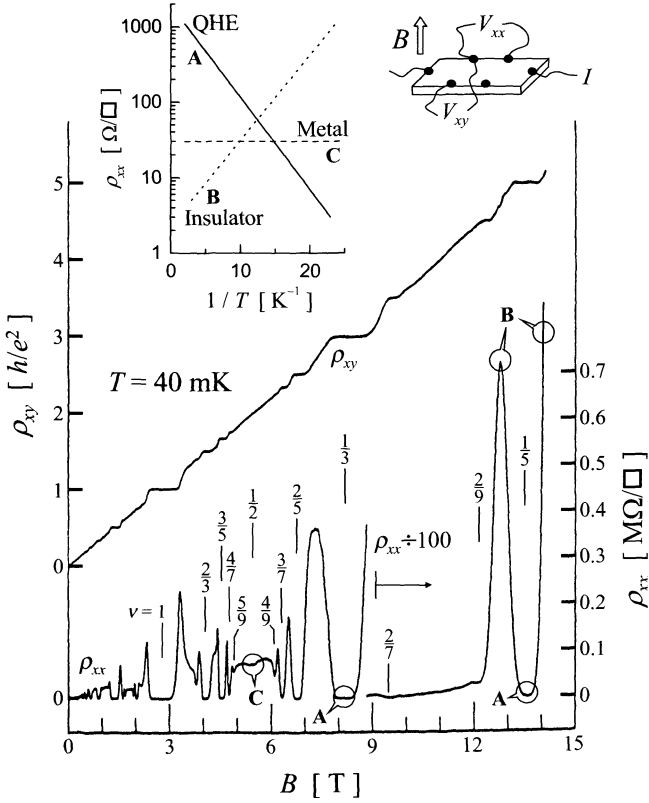
Fig. 1. Low-temperature magnetotransport coefficients of a high-quality (low-disorder) 2D electron system in a modulation-doped GaAs/AlGaAs heterostructure with a 2D density of 6.6×10^{10} cm^{-2}. The longitudinal (ρ_{xx}) and Hall (ρ_{xy}) resistivities at a temperature of 40 mK are shown in the main figure. The Landau-level filling factors (ν) are indicated by vertical markings. The right upper inset shows the typical measurement geometry while the left inset schematically illustrates the widely different temperature dependences of ρ_{xx} at different magnetic fields (filling factors).

to von Klitzing for the integral QHE (IQHE) [1,2], and another in 1998 to Laughlin, Stormer and Tsui for the fractional QHE (FQHE) [3,4], but surprises don't seem to stop.

Although both IQHE and FQHE have been studied extensively since their discoveries (see *e.g.* [5-8]), there have been a number of significant developments in recent years. These developments, on the one hand, have unveiled new subtleties of the basic QHE and on the other hand, have led to a more global and unifying picture of the physics of the 2DES at high

magnetic fields. Among these are the descriptions of the 2DESs at high B in terms of quasi-particles which consist of electrons and magnetic flux. The flux attachment treatment, which is based on Chern-Simons gauge transformation, maps the 2DES at high B onto a *Fermionic* or *Bosonic* system at a different, *effective*, magnetic field B_{eff}. Such mappings provide elegant explanations, as well as predictions, for some of the most striking, observable QHE phenomena. Examples include the existence of a Fermi surface for the composite Fermions at $\nu = \frac{1}{2}$ filling where $B_{eff} = 0$, the similarity of the IQHE and FQHE, the transitions between QHE states and the transitions between QHE and insulating states at low fillings.

   The purpose of these notes is to provide a glimpse of some of the exciting recent experimental results in this field. I will focus on the following five areas; I will be very brief when covering these topics except in the part dealing with the bilayer systems, where I will go a bit more in depth:

1. a quick summary of some of the sample parameters and experimental aspects;

2. some basic and general remarks on the ground states of a 2DES in a strong magnetic field;

3. a simple magnetic focusing experiment near $\nu = \frac{1}{2}$ which provides a clear demonstration of the presence of a composite Fermion Fermi surface and the semiclassical, ballistic motion of the composite Fermions;

4. recent experimental results near the $\nu = 1$ QHE providing evidence for yet another set of quasi-particles, namely electron spin textures known as *Skyrmions*; and

5. *bilayer* electron systems in which the additional (layer) degree of freedom leads to unique QHE and insulating states which are stabilized by strong intralayer *and* interlayer correlations.

I'd like to emphasize that these notes cannot and do not deal with all the important and exciting aspects of the QHE and related phenomena. They provide only a limited and selective sample of recent experimental developments. Readers interested in more details are referred to the original papers as well as extensive review articles and books [1-8]. Also, there will be a minimal treatment of theory here; for more details and insight, I suggest reading the comprehensive and illuminating notes by Steve Girvin in this volume and those by Allan MacDonald in proceedings of the 1994 Les Houches Summer School [9].
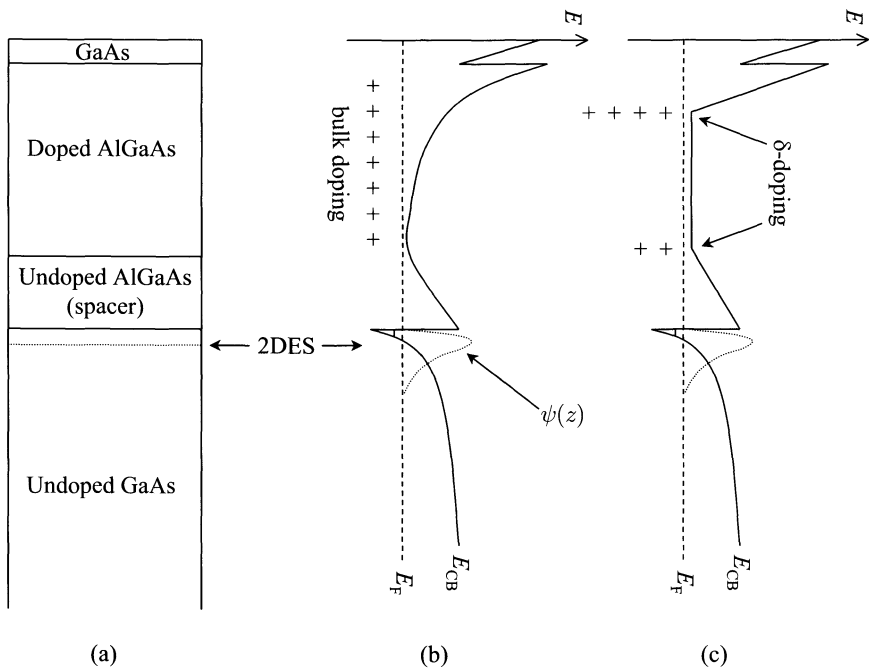
| (a) | (b) | (c) |

Fig. 2. Schematic description of a modulation-doped GaAs/AlGaAs interface. Since the conduction-band edge (E_{CB}) of GaAs lies lower in energy than that of AlGaAs, electrons transfer from the doped AlGaAs region to the undoped GaAs to form a quasi-2D electron system (2DES) at the interface. The 2DES is separated from the doped AlGaAs by an undoped AlGaAs (spacer) layer to minimize electron scattering by the ionized impurities. Note that the electron wavefunction, $\psi(z)$, has a finite extent in the direction perpendicular to the plane in which the electrons move freely. In (b) and (c) two common doping techniques are shown: bulk doping where the AlGaAs is uniformly doped and δ-doping where the dopants are themselves confined to a plane (to two planes in the structure shown in (c)).

2 Samples and measurements

2.1 2D electrons at the GaAs/AlGaAs interface

One of the simplest ways to place electrons in a flatland is to confine them to the interface between two semiconductors which have different bandgaps. An example is shown in Figure 2 where a 2DES is formed at the interface between undoped GaAs and AlGaAs. The larger bandgap of AlGaAs leads to its conduction-band energy (E_{CB}) being higher than GaAs. The system is "modulation-doped" [10] meaning that the dopant atoms (in this case,

Si donors) are placed in AlGaAs at some distance away from the interface. The electrons from the donors find it energetically favorable to transfer to the lower energy conduction-band of GaAs. But as they transfer, an electric field sets up between the positively-charged (ionized) donors in AlGaAs and the transferred electrons in GaAs. This electric field limits the amount of charge transfer. Figures 2b and 2c schematically show E_{CB} as a function of position, at equilibrium, after the charge transfer has taken place [11,12].

A key point in the structure of Figure 2 is that the 2DES is separated from the ionized dopants. As a result, the scattering of electrons by the ionized impurity potential is significantly reduced, meaning that the 2D electrons are essentially "free" to move in the plane. It turns out this is crucial for much of the phenomena that is observed in these systems: by reducing the disorder and the electron-impurity interaction, electrons are allowed to interact with each other, and the result is a host of new many-body ground and excited states. Another important message here is that although we call the system "two-dimensional", the electron wavefunction $\psi(z)$ spreads in the z direction by a finite amount, typically ~ 100 Å. This finite layer-thickness plays an important role and should be taken into account when comparing theoretical calculations and experimental results: it distinguishes between "ideal" 2D system assumed in many calculations and the "real" quasi-2D, experimental system.

How does one fabricate a structure like in Figure 2 and what are the details of a typical sample structure? Figures 3 and 4 provide schematic illustrations. The best quality GaAs/AlGaAs samples are presently grown by molecular beam epitaxy (MBE) [13]. The MBE system (Fig. 3) is essentially a very "clean" high-vacuum evaporation chamber. A GaAs substrate, heated to about 600 °C, is positioned in front of effusion cells (ovens) each of which contains one of the required elements (Ga, Al, As, and Si). The ovens are heated to appropriate temperatures to produce fluxes of these elements which can impinge on the GaAs substrate. Each oven also has a shutter which is controlled, often *via* a computer, to produce a desired structure such as the one shown in Figure 4. Under these circumstances, and with a growth rate of about one monolayer of GaAs per second (which is roughly 1 μm/hour), one can grow very high quality, *single-crystal* structures with nearly any design.

What determines the "quality" of the 2DES? For the electron-interaction-dominated phenomena in which we are interested here, the best sample is typically one with the least amount of imperfections such as interface irregularities, ionized impurities, *etc*. It is this consideration that leads to a complicated-looking structure such as the one shown in Figure 4. For example, the 2DES is separated from the Si dopants by a very thick spacer layer of undoped AlGaAs. The double-δ-doping is used to reduce the autocompensation of Si and to maximize the distance between
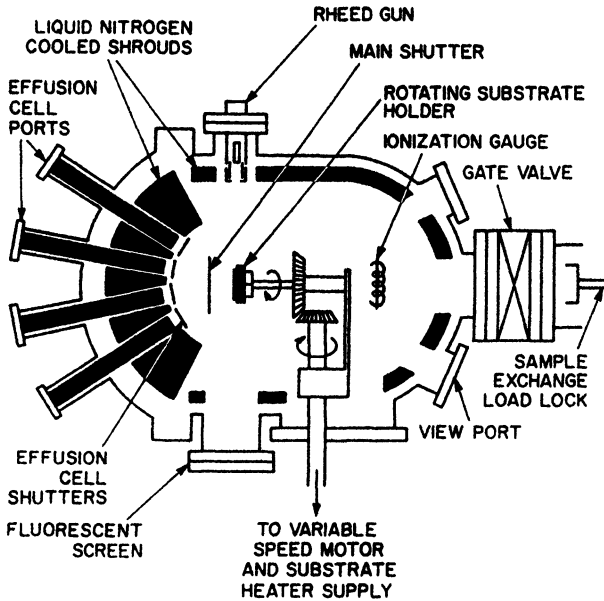
Fig. 3. Cross-sectional view of a molecular beam epitaxy (MBE) growth chamber (after Ref. [13]), essentially a very high-vacuum evaporation chamber with a base pressure of $\sim 10^{-14}$ atmosphere. The chamber is equipped with various vacuum pumps, such as ion-pumps and cryopumps, and also can have analytical equipment such as a reflection high-energy electron diffractometer (RHEED) to monitor *in-situ* the substrate surface morphology as well as growth rate.

the ionized dopants and the 2DES [14,15]. Details and rationale for other fabrication procedures such as growth interruptions, the use of spacer with graded Al composition, *etc.*, can be found in References 15 and 16. But a very important factor determining the quality of the 2DES, one which is not explicitly apparent in the structure of Figure 4, is the amount of residual (or unintentional) impurities that are incorporated *throughout* the structure during the MBE growth. These impurities are always present because the vacuum in the MBE chamber is not perfect, and also because the source materials (Ga, Al, *etc.*) used in the ovens are not 100% pure. It turns out in fact that in a structure like in Figure 4, with a large (> 2000 Å) spacer layer thickness, the most important factor in obtaining very low-disorder 2DES is the *purity* of the grown material and not the specific details of the structural parameters. The vacuum integrity of the MBE growth chamber and the cleanliness and purity of the source materials and the GaAs substrate are therefore of paramount importance for the fabrication of state-of-the-art 2DES.
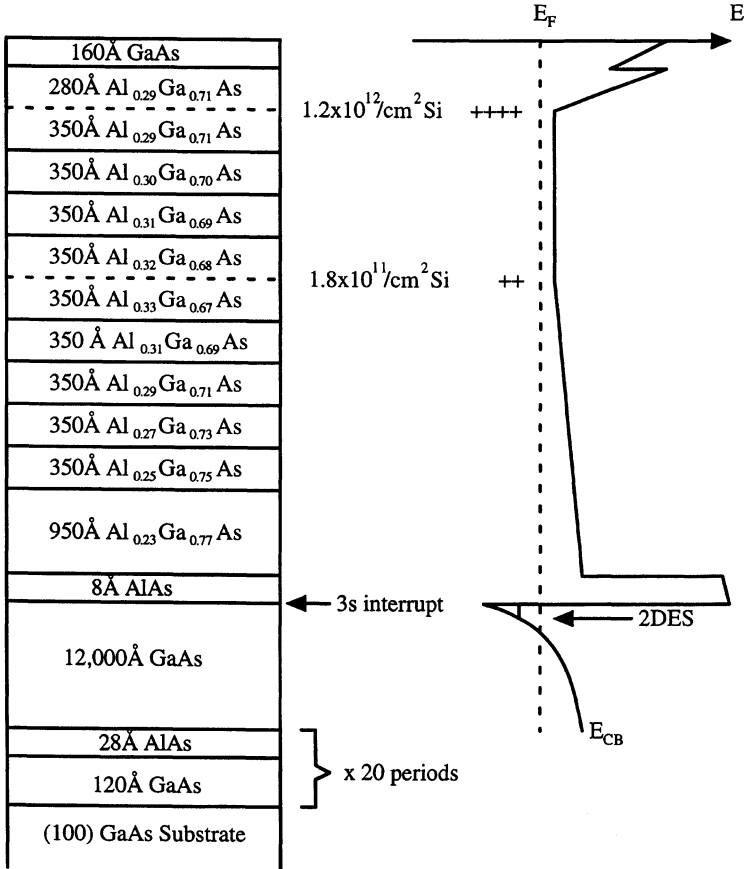
Fig. 4. Layer structure of a modulation-doped GaAs/AlGaAs heterojunction grown by molecular beam epitaxy (after Ref. [15]). The measured magneto-transport data for this sample are shown in Figure 1.

A measure of the electronic "quality" of a 2DES is its low-temperature mobility, μ. Over the years, the mobility of modulation-doped GaAs/AlGaAs heterostructures has improved tremendously and the record stands at about 10^7 cm^2/Vs for a 2DES density (n) of $\sim 2 \times 10^{11}$ cm^{-2}, implying a mean-free-path of tens of microns [17]. This mobility is more than $\sim 10^4$ times higher than μ for a uniformly-doped piece of GaAs, demonstrating the striking power of modulation-doping. As mentioned in the last paragraph, the mobility in such thick-spacer structures is in fact limited by the concentration of the non-intentional (residual) impurities. This is evidenced by the observation [16-18] that $\mu \sim n^\gamma$ with $\gamma \simeq 0.6$; this is the

dependence expected if the dominant source of scattering is the *residual impurities* in the close proximity of the 2DES [19]. The residual impurity concentration, deduced from the mobility values for state-of-the-art 2DES with $\mu \gtrsim 10^6$ cm^2/Vs for $n \gtrsim 5 \times 10^{10}$ cm^{-2} is $n_i \lesssim 1 \times 10^{14}$ cm^{-3}, consistent with the residual GaAs doping expected in very clean MBE systems. An $n_i \sim 10^{14}$ cm^{-3} means that the average distance between the residual impurities (~ 2000 Å) is smaller than the spacer layer thickness and, more importantly, is much larger than the typical inter-electron distance in the 2DES (~ 450 Å for $n = 5 \times 10^{10}$ cm^{-2}). Clearly in such low-disorder 2D systems it is reasonable to expect that the physics can be dominated by electron-electron interaction.

2.2   Magnetotransport measurement techniques

A variety of experimental techniques have been used to probe the electrical, optical, thermal, and other properties of the 2DES in a high magnetic field. The bulk of the measurements, however, have been on the magnetotransport properties. Magnetotransport measurements are also by far the main topic of this paper. I therefore briefly discuss such measurements here. In typical *dc* (or low-frequency, $\lesssim 100$ Hz) transport experiments, the diagonal and Hall resistivities are measured in a Hall bridge or van der Pauw geometry with ~1 mm distance between the contacts. Contacts to the 2DES are made by alloying In or InSn in a reducing atmosphere at ~ 450 °C for about 10 minutes. High-frequency measurements often involve more specialized geometries and contacting schemes. The low-T 2D carrier concentration can be varied by either illuminating the sample with a light-emitting diode or applying voltage (with respect to the 2DES) to a back- and/or front-gate electrode. Low temperatures are achieved using a ^{3}He/^{4}He dilution refrigerator, while the magnetic field is provided either by a superconducting solenoid or a Bitter magnet, or a combination of both. The low-frequency magnetotransport measurements are typically performed with a current excitation of $\lesssim 10^{-9}$ A, corresponding to an electric field of $\lesssim 10^{-4}$ V cm^{-1} and using the lock-in technique.

3   Ground states of the 2D system in a strong magnetic field

3.1   Shubnikov-de Haas oscillations and the IQHE

A large magnetic field applied perpendicular to the plane of a 2DES acts like a harmonic oscillator potential and leads to the quantization of the orbital motion. The allowed energies are quantized and are given by the "Landau Levels" (LLs), $(N + \frac{1}{2})\hbar\omega_c$, where $N = 0, 1, 2, ...$ and $\hbar\omega_c = \hbar eB/m^*$ is the cyclotron energy. For a system with a finite effective Lande g-factor (g^*), the energy spectrum is further quantized as each LL is spin-split to
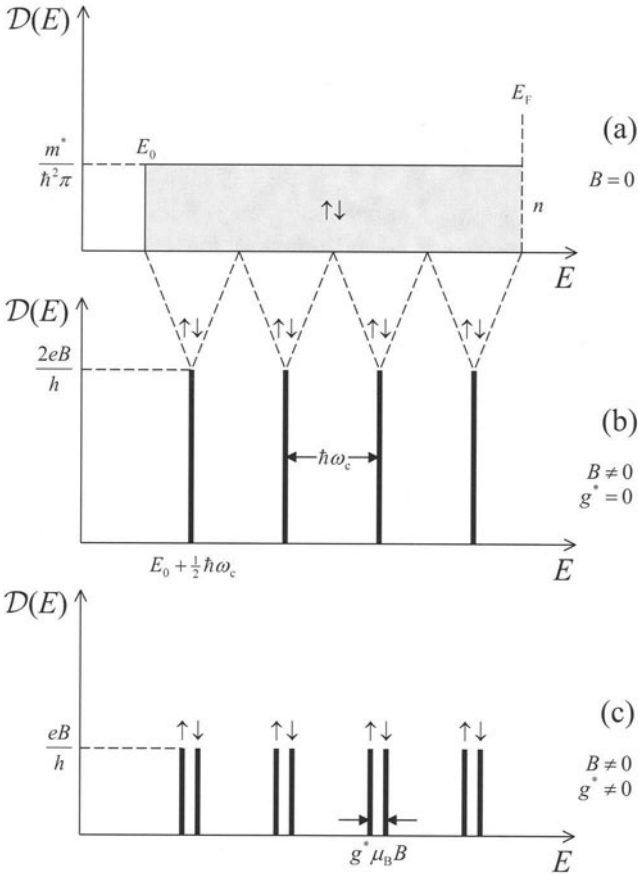
Fig. 5. Density-of-states as a function of energy for a 2D carrier system: (a) in the absence of a magnetic field, (b) with a magnetic field (B) applied perpendicular to the 2D plane but neglecting the spin-splitting of the resulting Landau levels, and (c) with spin-splitting included. As is typical for a 2D electron system in a standard, single GaAs/AlGaAs heterojunction, here it is assumed that only one (size-quantized) electric subband, whose edge energy is marked by E_o, is occupied.

two levels separated by the Zeeman energy $|g^*\mu_B B|$ where μ_B is the Bohr magneton. This evolution of the density-of-states, $D(E)$, for a 2D system in a magnetic field is schematically shown in Figure 5. Note that for 2D electrons in GaAs, $m^* = 0.067m_o$ and $g^* \simeq -0.44$, so that the cyclotron energy is about 70 times larger than the (bare) Zeeman energy.

The degeneracy of each spin-split quantized energy level is eB/h. Since this degeneracy increases with B, to keep the total 2D density (n) of

the system constant, the Fermi energy (E_F) has to move so that fewer and fewer LLs are occupied with increasing B. The number of spin-split LLs occupied at a given B is defined as the filling factor and is given by $\nu = n/(eB/h) = nh/eB$. Equivalently, ν is the number of electrons per flux quantum $\Phi_o = h/e$. As B is increased and E_F passes through the oscillating $D(E)$, nearly all properties of the system, such as electrical resistivity, magnetic susceptibility, heat capacity, *etc.*, oscillate. (The magnetoresistance oscillations are often called Shubnikov-de Haas oscillations.) The oscillations are periodic in $1/B$ with frequency nh/e or $nh/2e$, depending on whether or not the spin-splitting is resolved. This means that from a measurement of the frequency of the oscillations one can deduce the density. We will return to these oscillations in Section 6 where we analyze them to characterize the bilayer electron systems.

The delta-function-like energy levels shown in Figure 5 are for an ideally pure 2DES. In the presence of disorder, the levels are broadened with their width, Γ, being of the order of $\hbar/\tau_q$ where τ_q is the quantum lifetime of the carriers. The states in the LLs' tails are *localized* and only the centers of the LLs contain current-carrying *extended* states. Now suppose the filling factor is i, or nearly i, so that E_F lies in the localized states between the i and $i+1$ LL. If the disorder and temperature are sufficiently small so that Γ and $k_B T$ are both smaller than the LL separation, then as $T \to 0$ the longitudinal conductivity (σ_{xx}) vanishes and σ_{xy} becomes quantized at a value that is equal to ie^2/h. This is the integral QHE. That $\sigma_{xx} \to 0$ is simply a consequence of there being no extended states in the bulk of the 2D system to carry current. There are, however, i current-carrying "edge states" near the edge of the sample and this leads to σ_{xy} being quantized although demonstrating this quantization is more subtle (see, *e.g.*, Steve Girvin's notes). Note also that, according to the simple relations which convert the elements of the conductivity tensor to those of the resistivity tensor, $\rho_{xx} = \sigma_{xx}/\left(\sigma_{xx}^2 + \sigma_{xy}^2\right)$ and $\rho_{xy} = \sigma_{xy}/\left(\sigma_{xx}^2 + \sigma_{xy}^2\right)$. Therefore, $\sigma_{xx} = 0$ and $\sigma_{xy} = ie^2/h$ means that $\rho_{xx} = 0$ and $\rho_{xy} = h/ie^2$. This explains the experimental result in Figure 1 for the Hall bar sample shown in the inset.

To summarize, the IQHE is a consequence of: (1) the quantization of the 2D system's energy levels into a set of well-defined (but broadened) LLs with separation greater than $k_B T$, and (2) the presence of localized states in between these LLs. Note that no electron-electron interaction is needed to bring about or to explain the IQHE.

3.2 FQHE and Wigner crystal

Suppose B is sufficiently raised so that $\nu < 1$. At $T = 0$ the kinetic energy of the 2DES is quenched and the system enters a regime where, in the absence of disorder, its ground state is determined entirely by the electron-electron

interaction. In the infinite B limit, the system approaches a classical 2D system which is known to be an electron crystal (Wigner Crystal) with the electrons localized at the sites of a triangular lattice [20]. At finite B, the electrons cannot be localized to a length smaller than the cyclotron orbit radius of the lowest LL, or the magnetic length $l_B = (\hbar/eB)^{1/2} = (\nu/2\pi n)^{1/2}$, and the ground state is typically a gas or liquid. However, when l_B is much smaller than the average distance between electrons, *i.e.* when $\nu << 1$, a crystalline state is possible [21]. We will return to this crystalline state shortly.

   A competing ground state of the 2D system at high B is the FQH liquid [3,4]. Ironically, the work that led to the discovery of the new and totally unexpected FQH phenomenon [3] was itself one of the early experimental searches for the magnetic-field-induced Wigner crystal! The FQHE, observed at the principal fillings $\nu = 1/q$ and other rational fractional fillings $\nu = p/q$ (q=odd integer) is characterized by the vanishing of ρ_{xx} and the quantization of ρ_{xy} at $(q/p)\left(h/e^2\right)$ as $T \to 0$. The effect is phenomenologically similar to the IQHE but its origin is very different. The FQHE state is an intrinsically many-body, incompressible quantum liquid, described by the Laughlin wavefunction:

$$\Psi_m^\nu \sim \prod_{i,j}(z_i - z_j)^m \times \exp\left(-\sum_i \frac{|z_i|^2}{4l_B}\right).$$

Here z_i and z_j are (complex) coordinates of pairs of electrons in the plane, and $m = 1/\nu$ is an *odd* integer so that the wavefunction is antisymmetric when two electrons are interchanged (Pauli exclusion principle). Note also that the Coulomb repulsion between electrons is built into this wavefunction as it becomes small when two electrons come close to each other. The wavefunction has strong short-range correlation but it does not describe a crystalline phase as it has no long-range order (see the "snap shots" shown in Fig. 12 of Steve Girvin's notes).

   The FQHE has many fundamental and interesting characteristics among which we briefly mention three here. First, the incompressibility implies that the ground state is separated from its excitations by a finite energy gap, Δ. Experimentally Δ can be measured from the activated T-dependence of ρ_{xx} according to $\rho_{xx} \sim \exp\left(-\Delta/2k_BT\right)$. This is superficially similar to the energy gap between the LLs which leads to the IQHE, but the origin of the FQHE gap is entirely many-body. The theoretical Δ for the $\nu = \frac{1}{3}$ FQHE in an *ideal* 2DES, with no disorder, zero layer-thickness, and infinitely separated LLs, is $\sim 0.1e^2/\varepsilon l_B$, where ε is the dielectric constant of the host material (GaAs). In *real* samples, however, the ubiquitous disorder, finite-layer thickness, and LL mixing lead to a gap which is much smaller than $0.1e^2/\varepsilon l_B$ (see, *e.g.*, Ref. [22]). Finite layer thickness, for example, leads to

a softening of the short-range Coulomb interaction, and results in the weakening of the FQHE. In fact, experiments [23] and calculations [24] have revealed that once the layer thickness exceeds $\sim 3l_B$, the FQHE quickly collapses.

A second, quite intriguing yet fundamental feature of the FQHE is that its elementary excitations carry fractional charge $e^* = e/m$ (see Steve Girvin's notes for details and insight). There have been several reports of measuring this fractional charge, the latest being measurements of the quantum shot noise which is proportional to the charge of the conducting carriers [25]. In these measurements, the current noise was monitored as a function of the backscattered current which results from the tunneling between the FQHE edge states in a point-contact (constriction). The results near $\nu = \frac{1}{3}$ indeed reveal that the current carrying particles have charge $e/3$.

The third noteworthy feature is the existence of FQHE states not only at the primary fillings $\nu = \frac{1}{3}$ and $\frac{1}{5}$, but also at a host of other odd-denominator fillings. Examples are the states at $\nu = \frac{2}{5}, \frac{3}{7}, ...$ and $\nu = \frac{3}{5}, \frac{4}{7}, ...$ which can be seen in Figure 1. The strength of these states, namely their measured energy gaps, typically decreases as the denominator of their filling gets larger. Also, they appear to form a sequence of decreasing strength as one goes from the primary state, such as $\nu = \frac{1}{3}$, towards the even-denominator filling $\left(\nu = \frac{1}{2}\right)$ at which there is no FQHE state.

These observations led to an explanation for the higher order FQHE states based on a "hierarchical" scheme where each state is considered the "parent" state for the adjacent (in filling factor) weaker state. The idea is that as one deviates from the exact filling for a given FQHE state, quasiparticles are created above the energy gap; these quasiparticles then interact and form an incompressible liquid once their density to magnetic flux ratio reaches certain values. Such a hierarchical construction can generate all the odd-denominator fractions, and explains certain features of the observed FQHE sequences. However, it fails to account for the observed strength/weakness of all FQHE states. Also, in this scheme, the wavefunctions of the higher order states turn out to be much more complex than those for the primary states at $\nu = \frac{1}{m}$ (m an odd integer). Moreover, such description of the FQHE differs entirely from that of the IQHE while it is hard to overlook the striking similarity between the FQHE sequence, e.g., at $\nu = \frac{1}{3}, \frac{2}{5}, \frac{3}{7}...$ and the IQHE sequence at $\nu = 1, 2, 3, ...$ In fact, if we "slide" the $5.5 < B < 9$T portion of the magnetoresistance trace in Figure 1 to the left so that the position of $\nu = \frac{1}{2}$ is now the "zero" of (effective) magnetic field, we can see a one-to-one correspondence between the above IQHE and FQHE sequences, both in terms of the field positions of ρ_{xx} minima and their relative strength. (This is true if we assume that the 2DES is fully spin-polarized at all fields.)

   Such observations prompted the search for a description of the QHE
which somehow links the integral and fractional effects. This has culmi-
nated in a remarkable description in which an even number of fluxes com-
bine with an electron to form a new, "composite" Fermion (CF) [26]. The
electron-electron interaction and the large magnetic field are embedded in
this flux-electron quasiparticle so that the system now behaves as if it con-
tains (essentially) non-interacting particles moving in an "effective" mag-
netic field which is the balance of the external field once the attached fluxes
are deducted. For example, focusing on the range $\frac{1}{3} \leq \nu \leq \frac{1}{2}$ and at-
taching two fluxes to each electron, the CF description maps the FQHE at
$\nu = \frac{1}{3}, \frac{2}{5}, \frac{3}{7}, ...$ to the IQHE at $\nu = 1, 2, 3, ...$ Perhaps even more intriguing
is the notion that the effective field at $\nu = \frac{1}{2}$ is zero for the CFs so that, at
$\nu = \frac{1}{2}$, they ignore the large external magnetic field and move about as if
there is no magnetic field. In fact, the CFs should have a Fermi surface at
$\nu = \frac{1}{2}$, just like electrons do at zero magnetic field!

   The CF description and its implications have recently been among the
most active areas in the physics of 2D systems at high B, both experimen-
tally and theoretically [26]. In Section 4, I will briefly describe a simple
experiment probing the Fermi surface of CFs.

   A few words regarding the competition between the FQHE and Wigner
crystal (WC) are in order. It turns out that the Laughlin FQH liquid states
at $\nu = p/q$ are particularly robust and have ground state energies which
are lower than the WC state energy, at least for $\nu > \frac{1}{5}$. This is illustrated
in Figure 6 where the estimated energies are plotted as a function of ν (for
details of estimations see Refs. [27] and [28]). The downward "cusps" in
energy reflect the incompressibility of the FQHE states and the presence of
energy gaps which are proportional to the discontinuties in the derivative
of energy *vs.* ν. Also shown schematically in Figure 6 (dashed curve) is
the expected dependence of the WC ground state energy on ν. Theoretical
calculations predict that, in an ideal 2D system, the WC should be the
ground state for ν smaller than about $\frac{1}{6}$. It is evident from Figure 6 that
while at $\nu = \frac{1}{5}$ the FQHE can be the ground state, the WC state may win
as the filling deviates slightly from $\frac{1}{5}$. It is possible therefore to have a WC
which is reentrant around a FQH liquid state.

   The above picture has been used to rationalize the general current belief
that the insulating behavior observed around the $\nu = \frac{1}{5}$ FQHE in the best
quality GaAs/AlGaAs 2DESs is the signature of a pinned WC state. The
solid is presumably "pinned" by the disorder potential, and can be made
to slide if a sufficiently large electric field is applied. Such depinning would
result in a nonlinear current-voltage characteristic, consistent with numer-
ous measurements. The magnetic-field-induced WC crystal problem in 2D
systems has been studied extensively during the past ten years; for recent
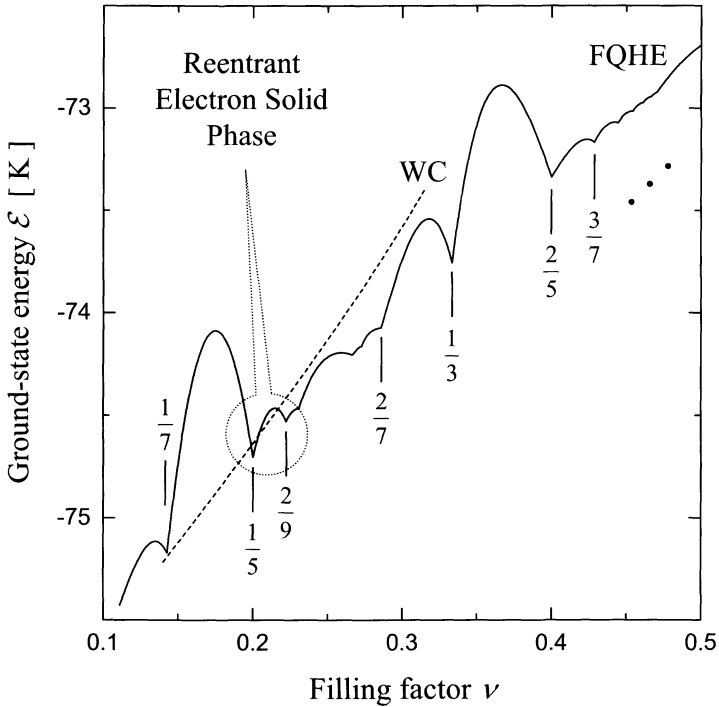reviews see reference [21].

Fig. 6. Energies of two competing ground states of a 2D electron system at high magnetic field. The FQHE incompressible liquid states occur at special odd-denominator fillings as the downward energy "cusps" indicate (solid curve). The Wigner crystal (WC) state has monotically decreasing energy as a function of inverse filling (dashed curve) and is expected to win for fillings less than about $\frac{1}{6}$. (After Ref. [28]).

4   Composite Fermions

Exploiting the transmutability of the statistics in 2D, a gauge transformation that binds an even number of magnetic flux quanta ($2m\Phi_0$ where m is an integer and $\Phi_0 \equiv h/e$ is the flux quantum) to each electron maps the 2DES at even-denominator fillings to a system of CFs at a vanishing B_{eff} [26]. Such transformation elegantly maps a FQHE observed at the 2DES filling ν to an IQHE for the CF system at filling ν' where $\nu' = \nu/(1 - 2m\nu)$. Moreover, since $B_{\text{eff}} = 0$ at $\nu = 1/2m$, the CF system should possess certain Fermi-liquid-like properties. Most notably, a CF Fermi surface should exist at and near $\nu = \frac{1}{2}$, supporting phenomena such as geometrical resonances and CF ballistic transport.
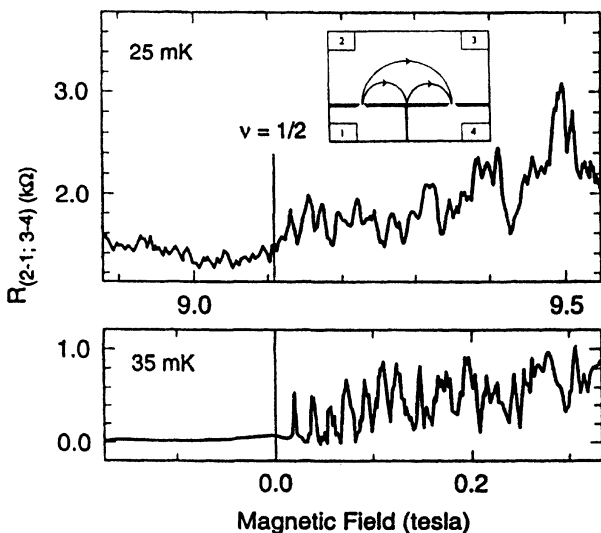
Fig. 7. Magnetic focusing spectra are shown for 2D electrons near zero external magnetic field (bottom trace) and for composite Fermions near $\nu = \frac{1}{2}$ (top trace) where the external field is about 9 T. In the top trace, the position of $\nu = \frac{1}{2}$ marks the zero of the effective magnetic field (B_{eff}) for CFs. Both traces exhibit peaks at fields where the distance between the injector and collector point-contacts ($L \simeq 5.3$ μm in this case) matches a multiple integer of the classical cyclotron orbit diameter. The inset schematically shows the top view of the sample. (After Ref. [29]).

Here I first present, as an example, the results of an experiment which provide a clear demonstration of the surprisingly simple behavior of CFs near $\nu = \frac{1}{2}$, namely their semiclassical, ballistic motion under the influence of B_{eff}. I then attempt to give a perspective of the field by listing some earlier, key experimental results and identifying current puzzles. For more details, I suggest reading more comprehensive review articles [26].

Figure 7 shows data from a magnetic focusing experiment [29] near $B = 0$ (bottom trace) and $\nu = \frac{1}{2}$ (top trace). The geometry of the experiment is sketched in the inset, which shows the top view of the sample. Parts of the sample are etched (thick lines in Fig. 7 inset) so that the 2DES is separated into three regions which are connected by two narrow constrictions (point-contacts). The distance between the two constrictions L, is chosen to be smaller than or of the order of the mean-free-path of the electrons. Ballistic electrons are then injected from the lower-left section to the upper section through the "injector" constriction by passing a current between the ohmic contacts 1 and 2. Now a small B-field is applied

perpendicular to the plane to "bend" the semiclassical, ballistic trajectory of the injected electrons as they travel in the upper section. As B is increased, whenever L matches a multiple integer of the electron's semiclassical cyclotron orbit diameter, $d_c = 2m^* v_F/eB = 2\hbar k_F/eB$, the ballistic electrons impinge on the "collector" constriction, either directly or after one or more bounces off the focusing barrier separating the two constrictions. At these B, one observes a maximum in the voltage measured between the lower-right and the upper sections (contacts 3 and 4). The traces shown in Figure 7 are the voltages measured between contacts 3 and 4, normalized to the current injected between contacts 1 and 2. Maxima can be clearly seen in the lower trace of Figure 7 for $B > 0$ and their positions are indeed consistent with the values of L and k_F for this 2DES. Note that for $B < 0$, the electrons are deflected to the left and no magnetic focusing is expected, consistent with the absence of any observed maxima.

The experiments of Goldman et $al.$ [29] reveal oscillations of the resistance not only near $B = 0$ for electrons, but also near $\nu = \frac{1}{2}$ (upper trace of Fig. 7). The data provide a remarkable demonstration of the "classical", ballistic motion of the CFs under the influence of B_{eff}. Note that B_{eff} is only a few tenths of a Tesla while the real external magnetic field is about 12 Tesla! The large external magnetic flux felt by the interacting electrons is replaced by the much smaller flux influencing the apparently simple flux-electron composites. The data of Figure 7 also provide a direct determination of the Fermi wavevector as well as an estimate for the ballistic mean-free-path of the CFs ($\simeq 1$ μm).

To bring the current status of the CFs into focus, I list some key experiments done so far (original references can be found in [26] or in [30]. These include measurements of the surface acoustic wave propagation, FQHE activation energies, CF effective mass, resistance oscillations in antidot arrays, magnetic focusing, low-T thermopower, magnetooptics, CF spin, temperature dependence of the CF conductivity at $\nu = \frac{1}{2}$ and $\frac{3}{2}$, and ballistic CF transport in nanostructures. The results of most of these experiments are in general agreement with each other and with the CF picture although some inconsistencies exist. Among the most controversial and hot current topics are the CF effective mass (m_{CF}^*) and the degree of CF spin polarization.

Theoretically, m_{CF}^* is expected to be strongly influenced by electron-electron interaction; it should be much larger than the bare ($B = 0$) electron effective mass, should scale with the Coulomb energy and therefore increase with B as $\sim B^{1/2}$ and may diverge as $\nu \to \frac{1}{2}$ [26]. While most experimental results agree with a rather large m_{CF}^*, there is no quantitative agreement. Neither is there an experimental consensus on the functional dependence of m_{CF}^* on B although most measurements agree with $\sim B^{1/2}$ dependence and some experiments have even reported a diverging m_{CF}^* as $\nu \to \frac{1}{2}$. The spin-polarization of the CFs near $\nu = \frac{3}{2}$ is also unclear. The surface acoustic

wave and antidot transport measurements suggest a spin-polarized state near $\nu = \frac{3}{2}$. The tilted-B magnetotransport measurements, however, are consistent with an unpolarized spin.

In summary, while there is now compelling experimental evidence for the validity of the CF picture of the FQHE, important uncertainties regarding the properties of these fascinating composite particles still remain.

5   Ferromagnetic state at $\nu = 1$ and Skyrmions

For 2DESs in GaAs, while the IQHE at even ν arises from the single-particle energy gaps separating the LLs, the spin splitting of these levels leads to IQHE at odd ν. The electron-electron interaction and in particular the exchange energy, however, play a dominant role for odd-ν IQHE and often lead to a substantially larger QHE energy gap than expected from the bare effective g-factor ($g^* \simeq -0.44$) for GaAs [31]. In fact, according to theory [32], the odd-ν IQHE states should exist even in the limit of zero Zeeman energy ($g^* \to 0$); there should be a spontaneous ferromagnetic order with a spin polarized 2DES ground state.

Perhaps even more interesting are the predicted excitations of these ferromagnetic states: provided that g^* is sufficiently small, the charged excitations of the system are finite-size "Skyrmions", termed so after the work of Skyrme in 1958 [33], rather than single spin flips. Skyrmions are spin textures, smooth distortions of the spin field involving several spin flips [32,34]. The spin and size of the Skyrmions are determined by the competition between the Zeeman and the exchange energies: a large ratio of the exchange energy over the Zeeman energy would favor large-size Skyrmions over single spin flips as the (exchange) energy gained by the near parallelism of the spins would outweigh the (Zeeman) energy cost of the extra spin flips. Skyrmions are relevant at $\nu = 1$ (at finite T) and near $\nu = 1$ where the 2DES is not fully spin polarized

Clear experimental evidence for finite-size Skyrmions was recently provided by the pioneering nuclear magnetic resonance measurements of Barrett *et al.* [35]. On either side of $\nu = 1$, they observed a rapid drop of the Knight-shift of the ^{71}Ga nuclei which are in contact with or are near the 2DES. Associating this Knight-shift with the spin polarization of the 2DES, they deduced that the charged excitations of the $\nu = 1$ QHE carry large ($\simeq 4$) effective spins [35]. Subsequent theoretical calculations have shown excellent quantitative agreement with the Knight-shift data and the spin polarization of the 2DES, thereby providing additional credence to the Skyrmionic picture near $\nu = 1$ [36]. Finally, magnetotransport [37] and magnetooptical [38] data have provided further evidence for Skyrmions and their size.

Implied by the Knight-shift data [35,39] is a strong coupling of the nuclear and 2DES spin systems near $\nu = 1$ where Skyrmions are present. Here I would like to discuss some recent 2DES heat capacity (C) data near $\nu = 1$ at very low T [40] which dramatically manifest the consequences of this Skyrmion-induced coupling. Moreover, a remarkably sharp peak observed in C *vs.* T is suggestive of a phase transition in the electronic system, possibly signaling a crystallization of the Skyrmions at very low T.

Bayot *et al.* [40] have succeeded in measuring C *vs.* B and T in a multiple-quantum-well sample in the QHE regime and at very low T (down to 25 mK). Their C *vs.* B data, shown in Figure 8, is striking in that at high B (near $\nu = 1$) C becomes many orders of magnitude larger than its low B value. Figure 9 reveals yet another intriguing feature of their data; in a small range of ν near 0.8 (and also near 1.2), C *vs.* T exhibits a very sharp peak at a temperature T_c which sensitively depends on ν (T_c quickly drops as ν deviates from 0.8 or 1.2) [40].

The low B data of Figure 8a can be understood based on the 2DES electronic heat capacity and its oscillating density of states at the Fermi energy [40,41]. The high B data (Figs. 8b and 9) near $\nu = 1$, on the other hand, are unexpected and cannot be accounted for based on the thermodynamic properties of the 2DES alone. Both the very large magnitude of C and the T^{-2} dependence of C at high T (dashed line in Fig. 9) hint at the nuclear Schottky effect. Utilizing this clue, Bayot *et al.* were able to semi-quantitatively explain the magnitude and the dependence of C on B and T (for $T > 0.1$ K) based on a simple Schottky model for the nuclear spins of the Ga and As atoms in the quantum wells. Implicit in this interpretation of course is a coupling between the nuclear spins and the lattice; this coupling is assumed to be provided by the Skyrmions.

The Schottky model, however, predicts a smooth maximum in C at $T \sim \delta/2k_B \simeq 2$ mK for $B \simeq 7$ T and cannot explain the sharp peak observed at $T_c \sim 35$ mK (δ is the nuclear spin splitting). It is possible that this peak may be a signature of the expected Skyrmion crystallization and the associated magnetic ordering near $\nu = 1$ [40,42,43]. Such crystallization has indeed been proposed theoretically [36,43] although the details of the Skyrmion liquid-solid transition and, in particular, how it would affect the coupling to the nuclear spin system are unknown. One feature of the data that qualitatively agrees with the Skyrmion crystallization is worth emphasizing. As shown in the upper inset in Figure 9, the observed T_c decreases rapidly as ν deviates from 0.8 or 1.2 [40]; this is consistent with the expectation that as the Skyrmion density decreases, the Skyrme crystal melting T should decrease.
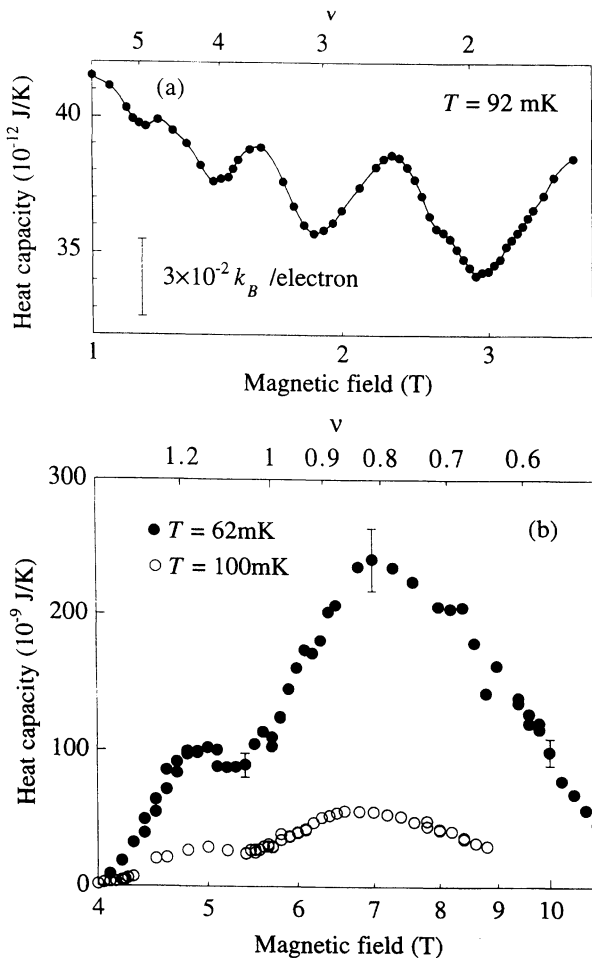
Fig. 8. Heat capacity C of a multiple-quantum-well sample, showing orders of magnitude enhancement of the high-B data (b) over the low-B data (a). The line through the data points is a guide to the eye. (After Bayot *et al.* [40].)

6 Correlated bilayer electron states

6.1 Overview

The introduction of an additional degree of freedom can have a profound effect on the many-body ground states of the 2DES at high B. For example, the addition of a spin degree of freedom stabilizes particular spin-unpolarized FQHE observed at lower B [44,45], while substantially
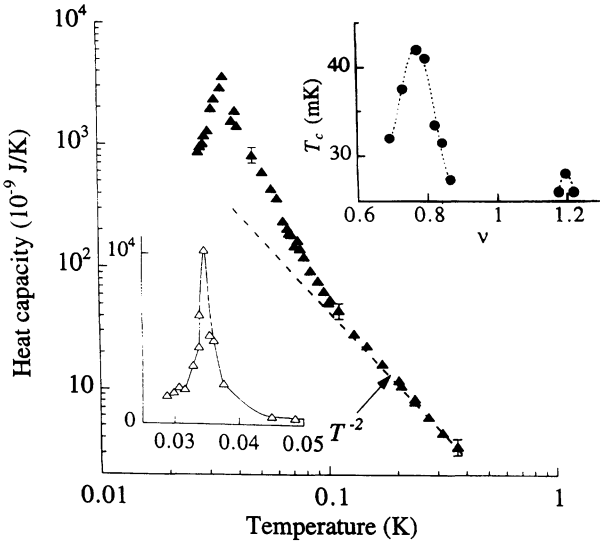
Fig. 9. The temperature dependence of C at $B = 7$ T ($\nu = 0.81$) is shown in the main figure in a log-log plot. The dashed line shows the T^{-2} dependence expected for the Schottky model. The lower inset shows a linear plot of C vs. T at $B = 6.7$ T ($\nu = 0.85$). The temperature T_c, at which the heat capacity exhibits the sharp peak depends on the filling factor as shown in the upper inset. (After Bayot *et al.* [40].)

increasing the layer thickness (thus introducing an additional spatial degree of freedom) leads to a weakening and eventual collapse of the FQHE [23,24].

In this section, I'd like to review magnetotransport results, obtained primarily in my laboratory at Princeton University, on a novel *bilayer* electron system. The data show how the additional (layer) degree of freedom results in new correlated states. We have been studying an electron system, confined in a wide GaAs quantum well, which can be tuned from a single-layer-like (albeit thick) system to a bilayer system by increasing the electron density n in the well [46]. This evolution with n and, in particular, the transition to a bilayer system where *interlayer* as well as intralayer interactions are dominant, has a dramatic effect on the correlated states of the electron system, as manifested in the magnetotransport data [47-51].

Figures 10 to 12 provide examples for an electron system in a 750 Å-wide GaAs quantum well. In certain ranges of n, there are well-developed FQH states at the *even-denominator* fillings $\nu = \frac{1}{2}$ [47-49,52] and $\frac{3}{2}$ [49] which have no counterparts in standard 2DESs in single-heterostructures. (Note that $\nu = \frac{1}{2}$ is the total filling for the system; it corresponds to 1/4 filling
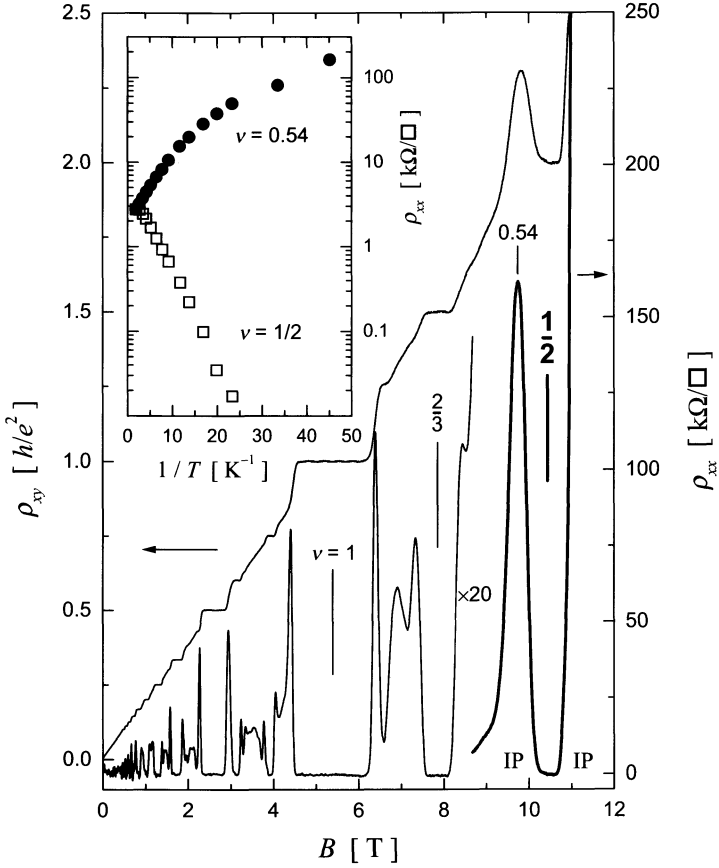
Fig. 10. Magnetotransport data, taken at $T \simeq 30$ mK, for a 750 Å-wide well with $n = 1.03 \times 10^{11}$ cm^{-2} (main figure) and $n = 1.55 \times 10^{11}$ cm^{-2} (inset), showing well-developed *even-denominator* FQH states at $\nu = \frac{1}{2}$ and $\frac{3}{2}$. These unique FQH states are stabilized by both interlayer *and* intralayer correlations. (After Suen *et al.* [49].)

for each layer). Figure 11 shows that at $n \simeq 1.26 \times 10^{11}$ cm^{-2}, insulating phases (IPs), which are *reentrant* around the $\nu = \frac{1}{2}$ FQH state, develop. The data of Figure 11 have a remarkable resemblance to the IPs observed in very high-quality, standard, single-layer, GaAs 2DESs (*e.g.*, see Fig. 1) except that here the IP is reentrant around the much higher filling $\nu = \frac{1}{2}$ rather than $\nu = \frac{1}{5}$! As we will discuss, the IPs of Figure 11 are suggestive of a pinned, *bilayer* Wigner crystal which is stabilized at high ν thanks to the *interlayer* correlation among electrons. Figure 12 demonstrates yet another surprising aspect of the QHE in this system. Here the Arrhenius plots of

Fig. 11. Data for the same sample of Figure 10 but with $n = 1.26 \times 10^{11}$ cm^{-2}. Here we observe an insulating phase (IP) reentrant around the $\nu = \frac{1}{2}$ FQH state. The inset shows the temperature dependence of resistivity: at $\nu = \frac{1}{2}$, ρ_{xx} vanishes as $T \to 0$ indicative of a FQH state while at slightly higher and lower ν, ρ_{xx} shows an insulating behavior as it diverges with decreasing T. (After Manoharan *et al.* [51].)

resistance at $\nu = 1$ as the density is varied are very unusual: the activated behavior of R_{xx} *vs.* $1/T$ starts rather abruptly below a temperature T^* which is much smaller than the deduced QHE gaps ($\simeq 20$ K) and, even more surprisingly, is *n-dependent*.

The evolution of the magnetotransport data in this system as a function of n, and the intriguing interplay between the incompressible liquid states (including the $\nu = \frac{1}{2}$ FQHE) and the IP, which displays behavior profoundly different from any observed in a standard 2DES, are the subject of this
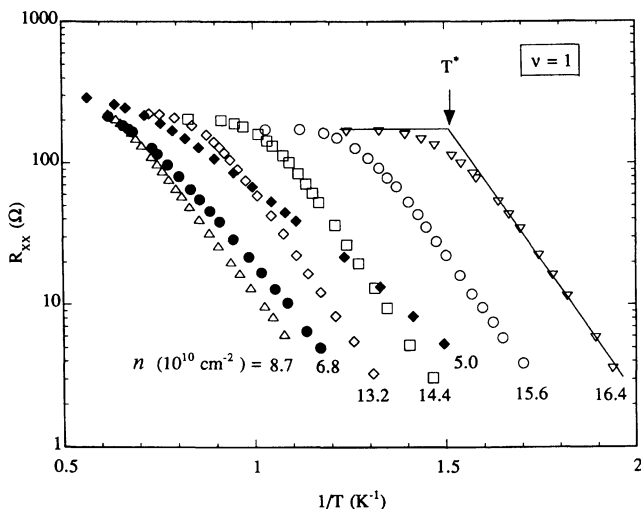
Fig. 12. Arrhenius plots of R_{xx} at $\nu = 1$ *vs.* $1/T$ for the sample of Figures 10 and 11 for different n. For $n > 10 \times 10^{10}$ cm^{-2}, the activated behavior of R_{xx} ends abruptly above a temperature T^* which strongly depends on n. (After Lay *et al.* [50].)

section. We will first give a brief overview of the sample structure and measurements in Section 6.2. Sections 6.3 and 6.4 summarize the evolution of the QHE and insulating states as the electron system is tuned from single-layer to bilayer. We will see that the *interlayer* as well as intralayer correlations play a key role in stabilizing the unique ground states of the system. In Section 6.5 we highlight our results for the $\nu = 1$ QHE in this system [50] and suggest that its very unusual dependence on T and n may be indicative of an unusual *finite-temperature* transition, from a QHE state to a compressible state, which is unique to interacting bilayer systems. Finally in Section 6.6 we present recent experimental results which reveal that a bilayer system with two equally-populated layers at zero magnetic field can spontaneously break its charge distribution symmetry through an interlayer charge transfer near the magnetic quantum limit [27]. New FQH states at unusual total fillings such as $\nu = \frac{11}{15} \left(= \frac{1}{3} + \frac{2}{5} \right)$ stabilize as signatures that the system deforms itself, at substantial electrostatic energy cost, in order to gain correlation energy by "locking in" separate incompressible liquid phases at unequal fillings in the two layers (*e.g.*, layered $\frac{1}{3}$ and $\frac{2}{5}$ states in the case of $\nu = \frac{11}{15}$).

6.2   Electron system in a wide, single, quantum well

The electron system in a wide, GaAs quantum well of width ~ 1000 Å is a particularly interesting one (Figs. 13 and 14). At low n the electrons occupy the lowest electric subband and have a single-layer-like (but rather "thick" in the z-direction) charge distribution (Fig. 13). As more electrons are added to the well, their electrostatic repulsion forces them to pile up near the well's sides and the resulting electron charge distribution appears increasingly bilayer-like. A relevant parameter that quantifies this evolution is the energy difference between the two lowest subbands which, for a symmetric charge distribution, corresponds to symmetric-to-antisymmetric energy splitting Δ_{SAS}; this is a measure of the coupling between the two layers. Also relevant is the interlayer distance, defined by the parameter d as shown in Figure 13. A crucial property of the electron system in a wide quantum well is that, for a given well width, both Δ_{SAS} and d depend on n: increasing n makes d larger and Δ_{SAS} smaller so that the system can be tuned from bilayer to (thick) single-layer by decreasing n (Fig. 13). This evolution with density plays a decisive role in the properties of the correlated electron states in this system.

Experimentally, we control both n and the charge distribution symmetry in the samples *via* front- and back-side gates (Fig. 15), and by measuring the occupied subband electron densities from Fourier transforms of the low-B magnetoresistance (Shubnikov-de Haas) oscillations (Fig. 16). One of the simplest ways to find the symmetric charge distribution at a given density n is to measure and minimize the subband separation (Δ_{01}) as a function of pairs of applied front- and back-gate biases while n is kept constant. The basic idea is that in our wide quantum well, as in a double-quantum-well, at a fixed n, Δ_{01} is smallest when the charge distribution is symmetric. In practice, we start with a given n and measure the subband densities from the Fourier transforms of the Shubnikov-de Haas oscillations (Fig. 16). Note that the difference between these densities can be simply converted to subband separation Δ_{01} by dividing by the 2D density of states $m^*/\pi\hbar^2$. Next we lower n by an amount Δn by applying a negative bias to the front-gate V_{FG} (with respect to an Ohmic contact made to the electron system), and then raise the density by the same amount Δn *via* the application of a positive bias V_{BG} to the back-gate. We then measure new subband densities. By repeating this procedure we can find the pair of V_{FG} and V_{BG} that results in the minimum measured Δ_{01}. This pair of V_{FG} and V_{BG} gives the symmetric ("balanced") charge distribution, and the minimum Δ_{01} is Δ_{SAS} at this n. Balanced states at a new density $(n + n')$ can now be achieved by changing one of the gate biases to reach $(n + n'/2)$ and the other gate to reach $(n + n')$ (n' can be positive or negative). The Δ_{SAS} data of Figure 13 were in fact obtained from Shubnikov-de Haas measurements on such "balanced" states, *i.e.*, the gates were tuned to preserve symmetric
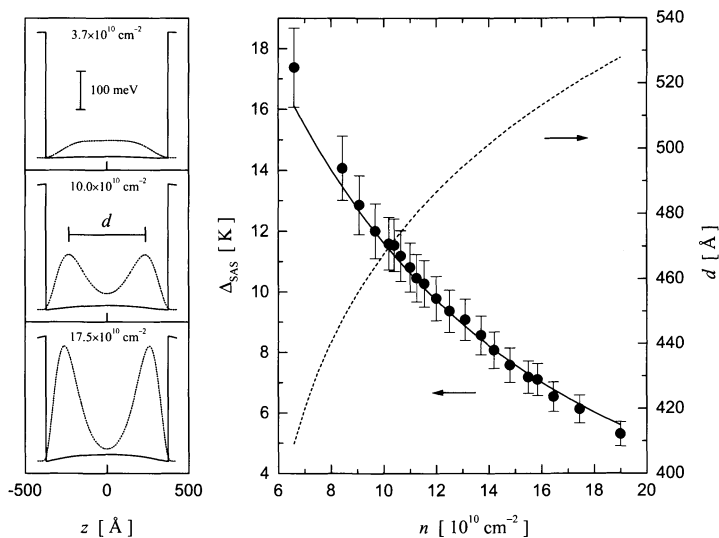
Fig. 13. The evolution of an electron system in a 750 Å-wide single quantum well as a function of total electron density n. On the left the results of Hartree-Fock simulations for the self-consistent conduction band potentials (solid curves) and charge distributions (dotted curves) are shown. On the right the calculated Δ_{SAS} (solid curve) is compared to the measured Δ_{SAS} (closed circles); also shown is the calculated layer separation d. (After Manoharan et al. [28].)

charge distributions in the well as shown in Figure 15a. The remarkable agreement of the data with the self-consistent calculations in Figure 13, and the controlled variation of Δ_{SAS} and d with n, attest to the excellent tunability of the electron system in a wide quantum well.

Besides this tunability, the bilayer electron system in a wide GaAs well has another great advantage over its counterpart in a double-quantum-well. Here the effective "barrier" separating the two electron layers is GaAs (Fig. 14) while in a double-quantum-well the barrier is AlGaAs or AlAs. The purity of GaAs grown in a molecular beam epitaxy chamber is typically higher than that of AlGaAs or AlAs (because of the high reactivity of Al and its sensitivity to impurities). Moreover, the AlGaAs or AlAs barrier in a double-quantum-well introduces additional interfaces which often adversely affect the quality of the electron system, e.g., because of the additional interface roughness scattering.
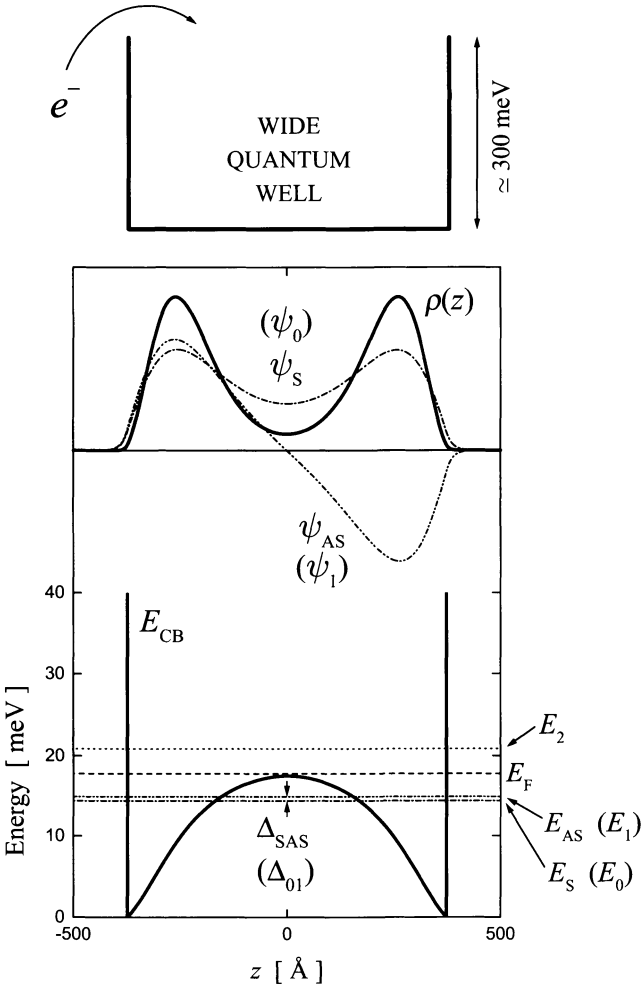
Fig. 14. Details of the potential, energy levels, and charge distribution in a 750 Å-wide GaAs quantum well with an electron density $n = 1.75 \times 10^{11}$ cm^{-2}. The potential (conduction-band edge, E_{CB}) is shown on top before any electrons are introduced. The main figure shows the results of self-consistent local-density approximation calculations, once the electrons are placed in the quantum well, for the potential and energy levels (bottom) and the wavefunctions and charge distribution (top). Note in the bottom figure that the effective "barrier" between the two electron layers is of GaAs and comes about because of the Coulomb repulsion between the electrons. The quantities in parentheses are for the general case when the system is not symmetric about $z = 0$. (After Manoharan [28].)
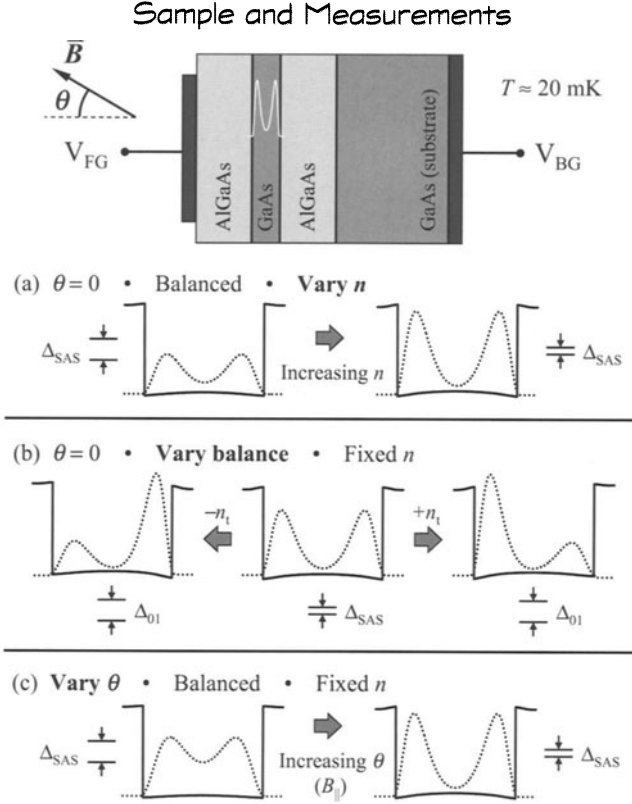
Sample and Measurements

Fig. 15. Summary of sample and measurement geometries. Top figure: The sample has front and back electrodes (gates) which can be biased by applying voltages (V_{FG} and V_{BG}) with respect to the electron system to change its density and charge distribution symmetry. (a) through (c) illustrate how in various measurements we can tune the bilayer system by varying three parameters, the density, the charge distribution symmetry or "balance" (characterized by density imbalance n_{t}), and the tilt angle between the direction of the magnetic field and sample normal. (After Manoharan [28].)

6.3   Evolution of the QHE states in a wide quantum well

Light is shed on the origin of the FQH states at $\nu = \frac{1}{2}$ and other fillings in a wide quantum well by examining the competition between (1) Δ_{SAS}, (2) the in-plane correlation energy $Ce/\varepsilon l_B$ [where C is a constant ~ 0.1 and $l_B \equiv (\hbar/eB)^{1/2}$ is the magnetic length], and (3) the interlayer Coulomb interaction $\sim e^2/\varepsilon d$. To quantify behavior it is useful to construct the ratios $\gamma \equiv \left(e^2/\varepsilon l_B\right)/\Delta_{\mathrm{SAS}}$ and $\left(e^2/\varepsilon l_B\right)/\left(e^2/\varepsilon d\right) = d/l_B$. As n is increased,
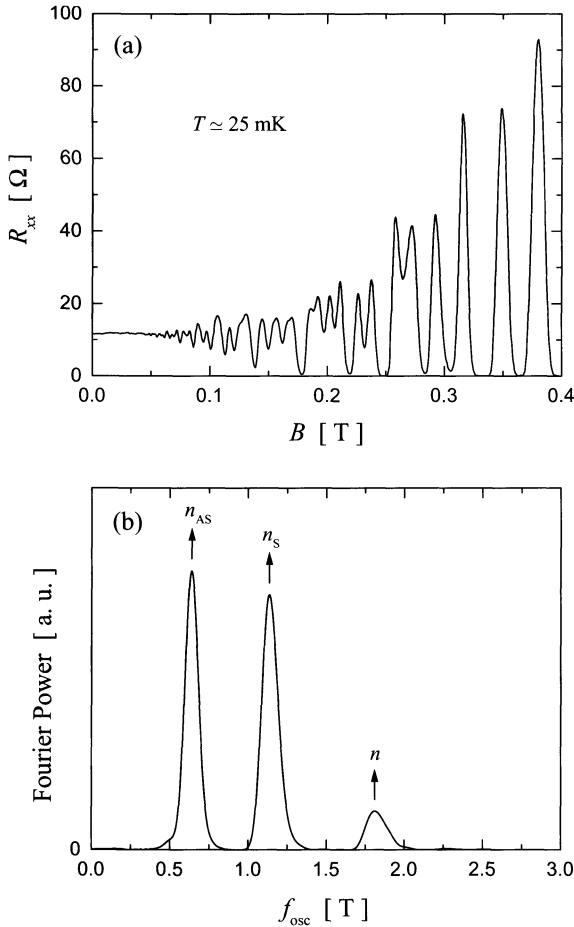
Fig. 16. Determination of subband gap from low-field Shubnikov-de Haas oscillations. Data are shown for a balanced charge distribution with $n = 8.8 \times 10^{10}$ cm^2. The oscillations, shown in (a), are periodic in $1/B$. Their Fourier power spectrum, shown in (b), exhibits two frequencies which can be converted to subband densities by multiplying by the (spin-degenerate) Landau level degeneracy ($2e/h$). The subband separation (Δ_{SAS}) can in turn be found by dividing the difference between these subband densities by the 2D density of states, $m^*/\pi\hbar^2$. (After Manoharan [28].)

γ increases since both Δ_{SAS} and l_B (for a FQH state at a given ν) decrease, and d/l_B increases. When γ is small, the system should exhibit only "one-component" (1C) FQH states (standard single-layer odd-denominator states) constructed from only the symmetric subband, while for large γ

the in-plane Coulomb energy becomes sufficiently strong to allow the an-
tisymmetric subband to mix into the correlated ground state to lower its
energy and a "two-component" (2C) state ensues. These 2C states, con-
structed out of the now nearly degenerate symmetric and antisymmetric
basis states, have a generalized Laughlin wavefunction of the form [53-56]:

$$\Psi_{mmn}^{\nu} \sim \prod_{i,j} (u_i - u_j)^m \prod_{i,j} (w_i - w_j)^m \prod_{i,j} (u_i - w_j)^n$$

$$\times \exp\left[-\sum_i \frac{|u_i|^2}{4l_B^2} - \sum_i \frac{|w_i|^2}{4l_B^2} \right], \tag{6.1}$$

where in a more intuitive, pseudo-spin or two-layer language, u_i and w_i
denote the pseudo-spin or the complex 2D coordinates of an electron in the
two layers. The integer exponents m and n determine the intralayer and
interlayer correlations, respectively, and the total filling factor for the Ψ_{mmn}^{ν}
state is $\nu = 2/(m+n)$.

Now the 2C states described by Ψ_{mmn}^{ν} come in two classes. For large
d/l_B, the system behaves as two independent layers in parallel, each with
half the total density. FQH states in this regime therefore have even nu-
merator and odd denominator. An example is the $\Psi_{330}^{2/3}$ state which has a
total filling of $\frac{2}{3}$ ($\frac{1}{3}$ filling in each layer). Note that the exponent $n = 0$
means that there is no interlayer correlation. For small enough d/l_B, on
the other hand, the interlayer interaction can become comparable to the
in-plane *(intralayer)* interaction and fundamentally new FQH states be-
come possible. Such states have strong interlayer correlation and can be
at even-denominator ν; a special example is the $\Psi_{331}^{1/2}$ state with $\nu = \frac{1}{2}$.
Another example is the Ψ_{111}^1 state at $\nu = 1$ which we will come back to in
Section 6.5. Figure 17 captures some of the possible 1C and 2C QHE states.

A careful study of the evolution of the FQH states in a wide quantum
well as a function of n reveals that this evolution is compatible with the
above picture [49]. Shown in Figure 18, for example, are three traces taken
at low, high and intermediate n. The trace at low n exhibits, besides the
usual integer QHE, the standard (odd-denominator) FQH states observed
in high-quality single-layer 2D systems. The FQH states observed in the
high n trace, on the other hand, while also having odd-denominators, have
predominantly *even-numerators* (exceptions are the QHE states observed
at $\nu = 1$ and at $\frac{11}{15}$, between $\frac{2}{3}$ and $\frac{4}{5}$ states, to which we will return in
Sects. 6.5 and 6.6 respectively). The trace taken at intermediate n is most
unusual as it appears to exhibit both single-layer FQH states (such as $\nu = \frac{3}{5}$)
and the unique, *even-denominator* $\nu = \frac{1}{2}$ FQH state.

Figure 19 provides a summary of the data taken at different n on this
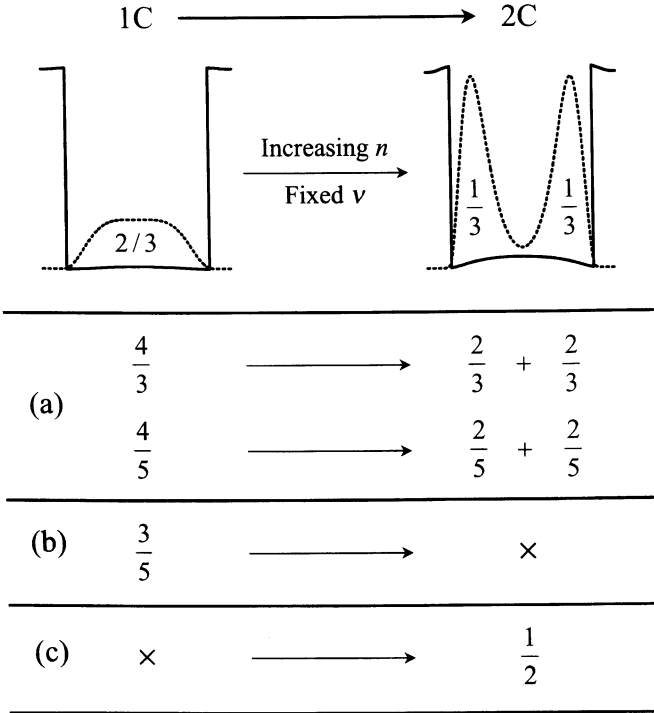sample. The quasiparticle excitation gaps of several FQH states, determined

1C $\longrightarrow$ 2C

Increasing n
Fixed ν $\longrightarrow$

2/3

$\frac{1}{3}$ $\frac{1}{3}$

(a) $\dfrac{4}{3}$ $\longrightarrow$ $\dfrac{2}{3} + \dfrac{2}{3}$

       $\dfrac{4}{5}$ $\longrightarrow$ $\dfrac{2}{5} + \dfrac{2}{5}$

(b) $\dfrac{3}{5}$ $\longrightarrow$ $\times$

(c) $\times$ $\longrightarrow$ $\dfrac{1}{2}$

Fig. 17. Examples of one-component (1C) and two-component (2C) FQH states in a wide quantum well. Numbers refer to the total filling factor ν of the electron system in the well. The even-numerator FQH states in (a) can exist in both single-layer and bilayer systems; in the bilayer case, they are essentially two independent FQH states in two parallel layers without interlayer correlation. The odd-numerator FQH state in (b) exists only in a single-layer system, while the even-denominator $\frac{1}{2}$ state is unique to bilayer systems and possesses interlayer correlation.

via thermal activation measurements, depend on γ as shown in this figure. As expected, increasing γ suppresses 1C states (such as $\frac{3}{5}$) and enhances 2C states (such as $\frac{4}{5}$). Two states, $\nu = \frac{2}{3}$ and $\nu = \frac{4}{3}$, undergo a 1C to 2C phase transition as γ is increased. The critical point for this transition, $\gamma \simeq 13.5$, is consistent with the ratio of the in-plane correlation energy and Δ_{SAS} $\left[\sim 0.1 \left(e^2/\varepsilon l_B\right)/\Delta_{\mathrm{SAS}} = 0.1\gamma\right]$ being of the order of unity, and matches the point where the energy gaps of other 1C and 2C states emerge from zero. Surrounding this point is a region where the $\nu = \frac{1}{2}$ FQH liquid stabilizes. Note that since this is a 2C state which also possesses interlayer correlation (the 2C $\nu = \frac{2}{3}$ and $\frac{4}{3}$ states are simply $\frac{1}{3}$ and $\frac{2}{3}$ states in parallel layers), it exists only within a finite range of γ.
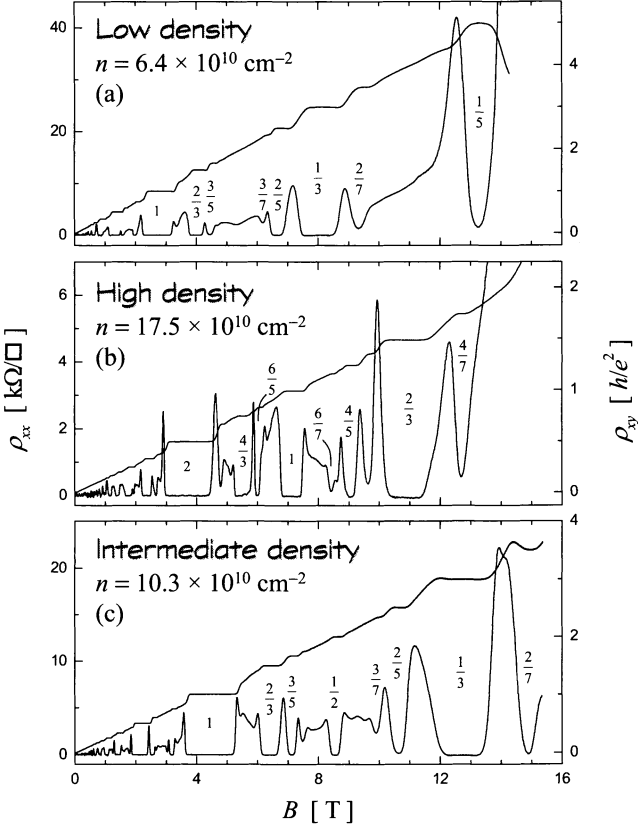
Fig. 18. Examples of QHE data in a 750 Å-wide quantum well, with balanced charge distribution, at three densities. The low-density data in (a) are essentially the same as in a high-quality, monolayer 2D electron system. The high density trace in (b) resembles what is observed in two parallel and independent layers as it exhibits primarily FQH states at fillings with even numerators and odd denominators (exceptions to these will be discussed in the text). At intermediate density (b), we have a bilayer system with strong interlayer interaction which leads to the stability of the new FQHE at $\nu = \frac{1}{2}$. (After Manoharan [28]).

A particularly interesting experiment is to study the effect of the charge distribution asymmetry on the FQH states observed in this system [28,49,57]. The results for the $\nu = \frac{1}{2}$ state are shown in Figure 20 where n is kept fixed at 1.03×10^{11} cm^{-2} but the charge distribution is made asymmetric by applying V_{FG} and V_{BG} in opposite polarities (Fig. 15b); here n_t is the electron density transferred from the back layer to the front layer. It can be seen that the $\nu = \frac{1}{2}$ FQH state quickly collapses as n_t is increased by a small amount. Note that increasing n_t means pushing the system to a single-layer
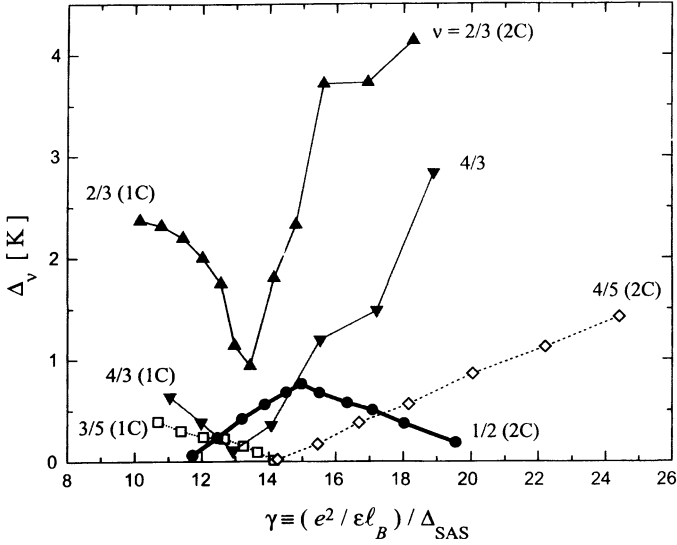
Fig. 19. Measured energy gaps Δ_ν of several FQH states *vs.* γ. The number of components (C) in each state is marked in parentheses. As γ increases, the 1C to 2C transition is observed at $\gamma \simeq 13.5$. The $\nu = \frac{1}{2}$ state is correlated both in the plane and between layers, and thus exists only within a finite range of γ. (After Suen [49] and Manoharan [28].)

(1C) situation; indeed, for $n_{\rm t} = n/2$ the system would become single-layer with all the charge residing in the front layer. (Note also that, as expected, the subband separation, Δ_{01} increases with $n_{\rm t}$.) These observations are consistent with the $\nu = \frac{1}{2}$ FQH state being a 2C state. For additional experimental results on the variation of FQHE energy gaps in this system with $n_{\rm t}$, see reference [49].

6.4 Evolution of insulating phases

Concurrent with the evolution of the FQH states in this wide quantum well, we observe an insulating phase (IP) which moves to *higher* ν as n is increased. The data are summarized in Figure 21 where ρ_{xx} at base T is plotted *vs.* $\nu^{-1} \propto B$ for several representative n. Experimentally, the IP is identified by a resistivity that is both large ($\rho_{xx} > h/e^2 \simeq 26$ k$\Omega/\square$, the quantum unit of resistance) [58], and strongly increasing as $T \to 0$ (see, *e.g.*, Fig. 11). For very low n, the IP appears near $\nu = \frac{1}{5}$, while at the highest n there is an IP for $\nu \lesssim \frac{1}{2}$. The IP observed in the intermediate density range $\left(10 \times 10^{10} < n < 14 \times 10^{10} \text{ cm}^{-2}\right)$ is most remarkable as it very quickly moves to larger ν with small increases in n (see, *e.g.*, traces **B**, **C**,
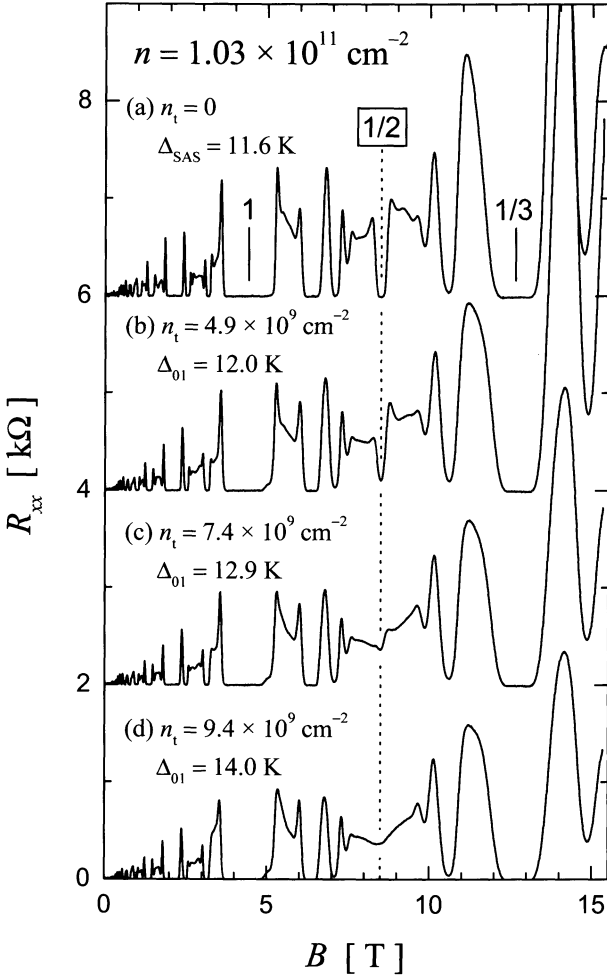
Fig. 20. Collapse of the $\nu = \frac{1}{2}$ FQHE state with asymmetry. In this experiment, total density is kept fixed at $n = 1.03 \times 10^{11}$ cm^{-2} while the charge distribution is made increasingly more asymmetric by applying front- and back- gate biases of opposite polarity [see Fig. 15b]. The $\nu = \frac{1}{2}$ FQHE is strongest when the charge distribution is symmetric but quickly weakens and eventually collapses as the layer charge imbalance n_t is increased. (After Suen [49,57] and Manoharan [28].)

and **D** in Fig. 21); along the way, it also shows *reentrant* behavior around well-developed FQH states at $\nu = \frac{2}{7}$ (trace **B**), $\nu = \frac{1}{3}$ (traces **C** and **D**), and $\nu = \frac{1}{2}$ (trace **E**). Then, as n increases past this point, the IP begins to move
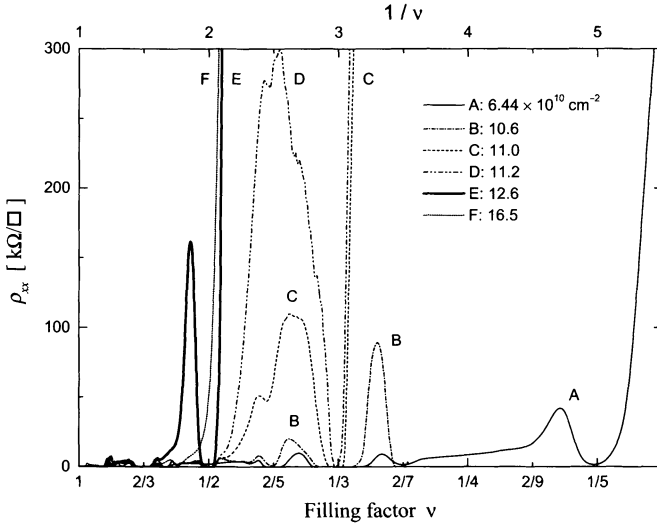
Fig. 21. Evolution of the insulating phase (IP) at $T \simeq 25$ mK. As n is increased, the IP moves quickly in to higher ν, becoming reentrant around several FQH states along the way, until it stabilizes around the $\nu = \frac{1}{2}$ bilayer state (bold trace **E**). As n is further increased from this point, the IP reverses direction and begins to move out toward lower ν. (After Manoharan *et al.* [51].)

in the opposite direction to lower ν (trace **F**). The data (trace **E**) shown in Figure 21 (see also Fig. 11) for $n = 12.6 \times 10^{10}$ cm^{-2} bear a striking resemblance to the IP observed reentrant around $\nu = \frac{1}{5}$ in low-disorder, single-layer 2DESs (Fig. 1), generally interpreted as a pinned Wigner solid [21]; here, however, the IP is reentrant around the bilayer $\nu = \frac{1}{2}$ FQH state, with the reentrant peak reaching the prominently high filling of $\nu = 0.54$.

The IPs presented in Figure 21 cannot be explained by single-particle localization. First, in the case of standard, single-layer 2DESs it is well known that as n is lowered, the quality of the 2DES deteriorates and the sample shows a disorder-induced IP at progressively larger ν [18]. This is opposite the behavior observed here: as n decreases from 10.9×10^{10} to 3.7×10^{10} cm^{-2}, the quality worsens as expected (*e.g.* mobility decreases monotonically from 1.4×10^{6} to 5.3×10^{5} cm^2/Vs) but the IP moves to *smaller* ν. Second, the observation of IPs which are reentrant around *correlated* FQH states, and particularly around the very fragile $\nu = \frac{1}{2}$ state [49], strongly suggests that electron interactions are also important in stabilizing the IP. We associate these IPs with pinned, *bilayer* Wigner crystal (WC) states which are stabilized at high ν thanks to the *interlayer* as well as intralayer electron correlation.

To illustrate that the behavior of this IP is indeed consistent with the WC picture, it is instructive to first examine the three main reentrant ρ_{xx} peaks in Figure 21 (from traces **B**, **D**, and **E**), which appear at $\nu = 0.30, 0.39$, and 0.54 for the IPs surrounding the $\nu = \frac{2}{7}, \frac{1}{3}$, and $\frac{1}{2}$ FQH states, respectively. The values of γ at these peaks are respectively 16.9, 16.3, and 16.5. The peak positions span a large region of ν, and yet the associated γ are remarkably similar. Moreover, at a γ of 16.5, interlayer interactions are clearly important as this point is straddled by the 2C $\frac{1}{2}$ state in Figure 19.

The construction of a phase diagram [51] for the observed IPs facilitates a clear correlation between the IP evolution, the 1C to 2C transition, and the development of the $\nu = \frac{1}{2}$ liquid. To this end, we first collected a ρ_{xx} data set for a fairly dense grid of points in the $n - B$ plane by incrementally changing n and sweeping B at base T. Next, ρ_{xx} was mapped to a color interpolating between blue $(\rho_{xx} = 0)$ and red $(\rho_{xx} \geq h/e^2)$. Finally, using the B, n, and Δ_{SAS} values at each point, the color-mapped ρ_{xx} data set was plotted *vs.* ν and γ (Fig. 22b; for the original color plot, see Ref. [51]). By utilizing h/e^2 as a natural resistivity scale for demarcating the IP and noninsulating states [58], the result is a comprehensive phase diagram depicting incompressible phases (dark blue) together with compressible phases, both insulating (dark red) and metallic (all other colors).

Immediately obvious in the phase diagram are the various FQH transitions, manifested by the appearance or disappearance of dark blue FQH phases at several ν (see, *e.g.*, $\frac{3}{5}, \frac{4}{5}$, and the $\frac{1}{2}$ "gulf"), or by a change in vertical width of the FQH phase (see, *e.g.*, $\frac{2}{3}$); these transitions correlate directly with the measured energy gaps (Fig. 22a). Another striking feature is the wrinkling in the IP boundary: this is caused by the aforementioned IP reentrance around several FQH states, perhaps most picturesque near $\nu \simeq 0.55$ due to the formation of an IP "peninsula" above the $\frac{1}{2}$ gulf. The limiting critical ν at low n (low γ) is close to $\frac{1}{5}$, consistent with a low-disorder monolayer 2DES (Fig. 1). For the highest n when the electron system is effectively two weakly coupled layers in parallel, one would expect (and measurements on wider quantum wells directly indicate) that the IP boundary moves to $\nu \simeq \frac{2}{5}$, consistent with two high-quality independent layers becoming insulating near $\frac{1}{5}$ filling in each layer. As our system is tuned through *coupled* layers, however, the IP boundary moves vividly above both of these limits to $\nu \simeq 0.55$, and then only at higher n does it begin to fall back toward the $\frac{2}{5}$ weak-coupling limit (lying outside the density limits of this sample).

We can examine in more detail the evolution of the IP as depicted in the phase diagram of Figure 22b by making comparisons to Figure 22a. For intermediate n, as γ increases, the IP first remains close to $\nu = \frac{1}{5}$ but then begins to move to higher ν in the range of $12 < \gamma < 15$. This range
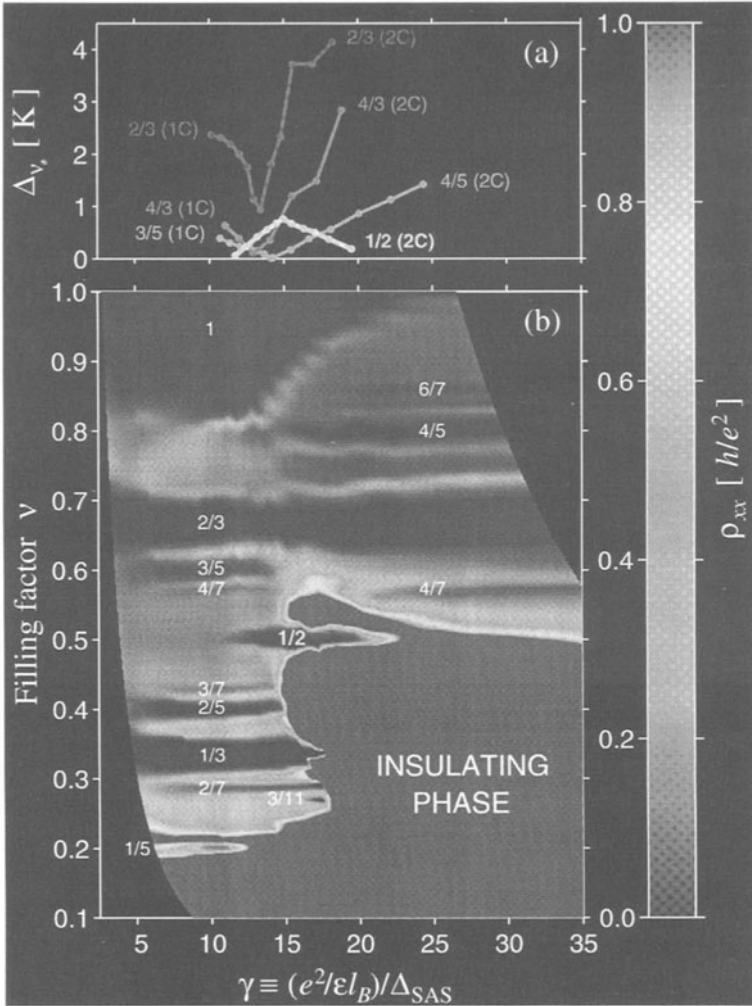
Fig. 22. (a) Measured energy gaps Δ_ν of several FQH states *vs.* γ. The number of components (C) in each state is shown in parentheses. (b) Phase diagram showing ρ_{xx}, chromatically mapped according to the color bar (right), *vs.* ν and γ. (After Manoharan *et al.* [51].)

is precisely bisected by $\gamma \simeq 13.5$ (Fig. 22a), where 1C to 2C transition occurs. Then the IP moves very quickly to $\nu \simeq \frac{1}{2}$ as evidenced by the nearly vertical phase boundary at $\gamma \simeq 16$. As discussed earlier, and as evident from Figure 22, this γ is centrally located in the parameter range in which the $\frac{1}{2}$ state stabilizes. A quick glance at the phase diagram underscores this
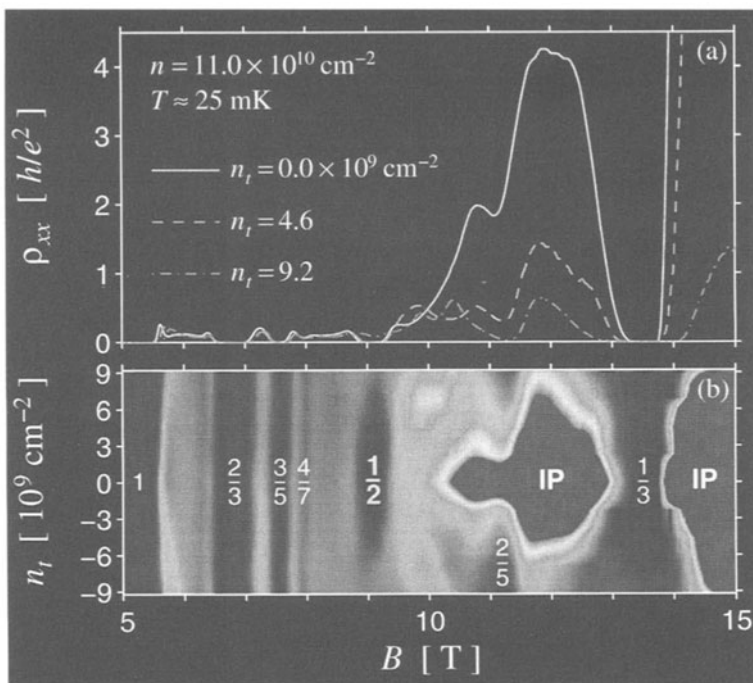
Fig. 23. phase (IP). Traces (a) and phase diagram (b) are at fixed total n, with varying amounts of charge n_t transferred between layers. [In (b), ρ_{xx} is mapped using the same color scale shown in Fig. 22.] Slight imbalance $|n_t|$ destabilizes the IP. (After Manoharan *et al.* [51].)

central point: the γ extent of the $\nu = \frac{1}{2}$ gulf coincides directly with the rapid ν shift in the phase boundary of the insulator.

The most convincing evidence for the formation of a pinned bilayer crystal comes from perturbing the symmetric ("balanced") charge distributions. Intuitively, the strength of a bilayer WC should be diminished under unbalanced conditions due to incommensurability effects. This is indeed observed quite prominently in our system, and can be highlighted by examining the high-ν reentrant IPs. Figure 23 shows the effect of asymmetry on the IP reentrant around $\nu = \frac{1}{3}$ at *fixed* $n = 11.0 \times 10^{10}$ cm^{-2} and for varying n_t, where n_t is the electron density transferred from the back layer to the front by proper gate biasing from the balanced condition. We construct an "imbalance" phase diagram by plotting ρ_{xx}, color mapped to the same scale shown in Figure 22 *vs.* n_t and B (Fig. 23b), and include in Figure 23a three representative ρ_{xx} traces (horizontal slices through the phase diagram of Fig. 23b). It is very clear that, while the 1C $\nu = \frac{1}{3}$ state is strengthened
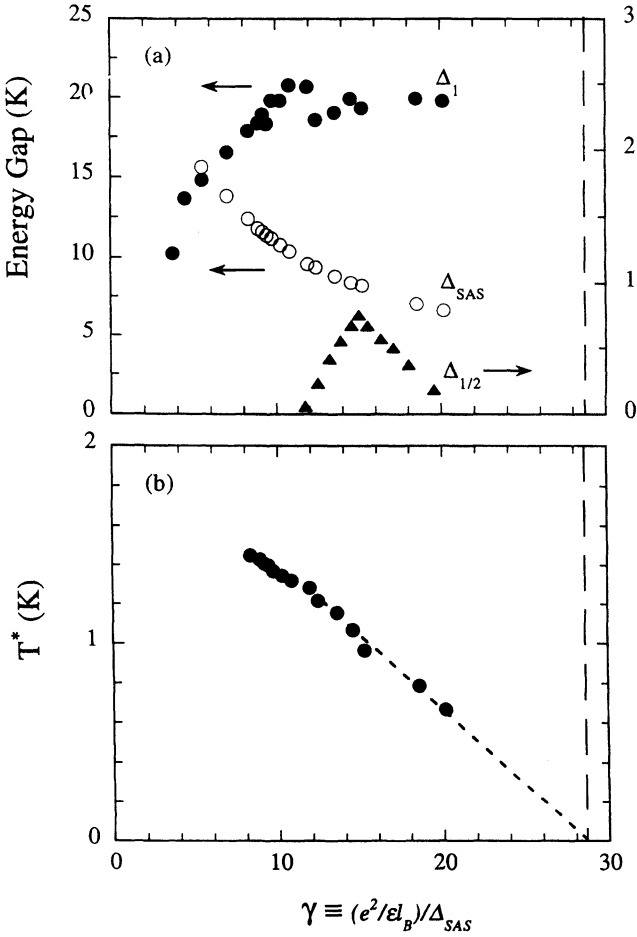
Fig. 24. Plots of the measured $\nu = 1$ QHE energy gap (Δ_1) and T^* *vs.* γ. The boundary for the collapse of the $\nu = 1$ QHE to a compressible state for this sample is shown by the vertical dashed line. As indicated by the dotted line, the measured T^* extrapolates to zero at this boundary. For comparison, the measured Δ_{SAS} and the $\nu = \frac{1}{2}$ QHE gap ($\Delta_{1/2}$) are also shown.

as expected, the IP is weakened by increasing imbalance $|n_t|$: The IP is most stable in a perfectly balanced state ($n_t = 0$) with a phase boundary at $B \simeq 10$ T, while the IP peak at $\nu = 0.38$ ($B = 12$ T) drops dramatically even for small imbalance $n_t = 4.6 \times 10^9$ cm^{-2} (Fig. 23a). As $|n_t|$ is increased past $\simeq 7 \times 10^9$ cm^{-2}, the reentrant IP is destroyed $\left(\rho_{xx} < h/e^2\right)$ and the $\frac{1}{2}$ FQH state disappears; the phase boundary (which has now jumped to

$B \gtrsim 14$ T) continues to be pushed back as n_t increase further (Fig. 23b). For the IP reentrant around $\nu = \frac{1}{2}$ at $n = 12.6 \times 10^{10}$ cm^{-2} (see Fig. 11), the corresponding destabilization of the insulator (not shown here) occurs at an imbalance of less than 3% ($|n_t| / n \simeq 0.027$). In all cases, note that both the $\nu = \frac{1}{2}$ FQH state and the reentrant IP are strongest in the balanced condition; asymmetry simultaneously destroys both the bilayer quantum Hall liquid *and* the insulator − for example, the vertical boundaries of the red reentrant IP "island" closely match those of the dark blue $\frac{1}{2}$ liquid phase (Fig. 23b).

Recently, several theoretical papers have examined Wigner crystallization in 2D systems with an additional spatial degree of freedom by considering multiple [59], wide [60], and double [61] quantum wells. While extracting details of the bilayer lattice (see, *e.g.* Ref. [61]) is beyond the scope of the present work, our observation of a 2C insulator at the large fillings we identify sharply resonates with the fundamental principle underlying these theoretical investigations [59-61]: there is an additional potential energy gain due to the interlayer Coulomb interaction so that for equivalent layer densities a 2C WC can form at higher ν (*e.g.*, $\nu \gg \frac{1}{5}$ per layer) than a 1C WC. In addition, interlayer coupling may concomitantly weaken the FQH effect, making a crossing of the liquid and solid ground-state energies even more favorable [23,60].

To summarize, our bilayer electron system provides a unique means of tuning the effective electron-electron interactions underpinning the formation of various many-particle ground states. The crux of this reasoning is that this system possesses two vital "yardsticks" for gauging the relative importance of interlayer and intralayer interactions: the 1C to 2C transition and the novel bilayer $\nu = \frac{1}{2}$ condensate. Utilizing these measuring sticks, we can connect the fascinating evolution of the IP with the significance and critical counterbalance of electron-electron interactions. In this light, the data conclusively indicate that the IP we observe for $\gamma \gtrsim 13$ is a collective 2C state with comparable interlayer and intralayer correlations. The characteristics of this bilayer electron insulator are remarkably consistent [59,60] with the formation of a novel pinned bilayer-correlated Wigner solid, a unique 2D electron crystal stabilized through the introduction of an additional quantum degree of freedom.

6.5   Many-body, bilayer QHE at $\nu = 1$

In bilayer systems with appropriate parameters, the interlayer interactions can also lead to *correlated* QHE at *integral* fillings [62]. A particularly interesting example is the 2C Ψ^1_{111} state at $\nu = 1$. In contrast to the 1C $\nu = 1$ QHE associated with Δ_{SAS}, the many-body, bilayer $\nu = 1$ incompressible state associated with Ψ^1_{111} has been predicted to exhibit exotic properties such as neutral superfluid modes and a Kosterlitz-Thouless

transition [63,64], and has already revealed an unexpected in-plane-B-driven transition (to another incompressible state) [65].

Data on electron systems in wide wells [50] reveal that in these systems the ground state at $\nu = 1$ evolves continuously from a QHE state stabilized by large Δ_{SAS} at low n to a many-body QHE state stabilized by strong interlayer interaction at intermediate n. As n is further increased, we observe an incompressible-to-compressible transition. The unusual T and n dependence of the data as the transition boundary is approached is suggestive of an additional *finite-temperature* transition from a QHE to a compressible state, which is unique to bilayer systems. Here we briefly summarize these data.

Figure 12 presents Arrhenius plots of R_{xx} at $\nu = 1$ for several n in our 750 Å-wide GaAs quantum well. The quasiparticle QHE excitation gaps Δ_1 determined from the slopes of the (low-T) activated regions of these plots, together with the measured and calculated Δ_{SAS} are shown in Figure 24a as a function of γ. For comparison, the gaps for the $\nu = \frac{1}{2}$ QH state in the same sample are also shown in Figure 24a. Several features of the data of Figures 12 and 24 are noteworthy: (1) while Δ_{SAS} decreases with increasing γ, Δ_1 increases and exceeds Δ_{SAS} by more than a factor of 3 at the highest measured γ. (2) For $n \gtrsim 10 \times 10^{10}$ cm^{-2} ($\gamma > 10$), the activated behavior of R_{xx} vs. $1/T$ starts rather abruptly below an n-dependent temperature T^*. Above T^*, the R_{xx} minimum at $\nu = 1$ vanishes, *i.e.*, R_{xx} becomes nearly independent of B and T. For $n \lesssim 10 \times 10^{10}$ cm^{-2} ($\gamma \lesssim 10$), however, the Arrhenius plots show a smoother behavior and Δ_1 gaps start to decrease with decreasing n. (3) The measured Δ_1 for $n > 10 \times 10^{10}$ cm^{-2} ($\gamma > 12$) are approximately constant (≈ 20 K) and exceed T^* by more than an order of magnitude. (4) A plot of the measured T^* vs. γ presented in Figure 24b, shows that T^* decreases with increasing γ and extrapolates to zero at $\gamma \simeq 29$. This γ corresponds to an incompressible-to-compressible phase boundary for $\nu = 1$ which we have observed in electron systems in a number of wide quantum wells with varying width [50]: in these systems, for sufficiently large γ, we observe a collapse of the $\nu = 1$ QHE to a compressible state. In the present sample, we cannot reach this boundary because the needed high n is not experimentally achievable but, based on our data on other samples, we expect the boundary to be at $\gamma = 29$ for this sample.

The above data demonstrate that the ground state of the electron system in this wide quantum well at $\nu = 1$ evolves continuously from a 1C QHE state at low n ($\gamma \lesssim 10$) stabilized by a large Δ_{SAS} to a 2C QHE state at intermediate n ($10 \lesssim \gamma \lesssim 20$), and then makes a transition to a metallic (compressible) state at large n ($\gamma > 29$). We believe that for intermediate n we are observing a bilayer QHE state stabilized by comparable interlayer and intralayer correlations, possibly a 2C, Ψ_{111}^1-like state [50]. Note in Figure 24a that in this density range, γ for the $\nu = 1$ QHE state overlaps
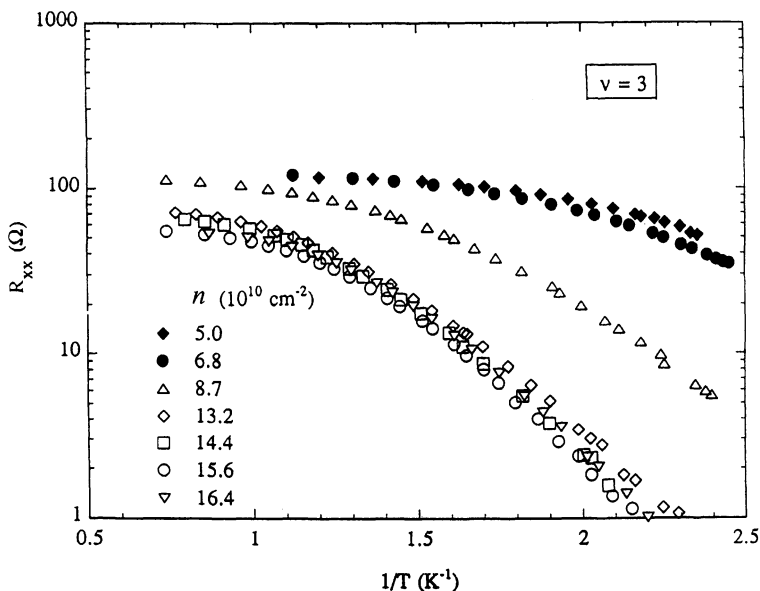
Fig. 25. Arrhenius plots of R_{xx} at $\nu = 3$ *vs.* $1/T$ for the sample of Figure 12. Note the very different and much smoother behavior of this data compared to the $\nu = 1$ data in Figure 12.

with γ of the $\nu = \frac{1}{2}$ QH state, a 2C liquid state which certainly requires interlayer correlations.

Finally, the data of Figures 12 and 24 are collectively very unusual and qualitatively different from what is observed for the integral or fractional QHE in standard, single-layer 2DESs, or for the QHE at higher fillings such as $\nu = 3$ in the *same* wide quantum well sample (Fig. 25). The single-layer $\nu = 1$ QHE data typically exhibit a smoother saturation of the activated behavior at high T and, as n is lowered, they show a larger R_{xx} (at any given T) and a smaller excitation gap [66]. This behavior is very similar to what we observe for the $\nu = 3$ QHE in this sample (Fig. 25) and for the $\nu = 1$ QHE at *low* n $\left(< 10 \times 10^{10} \text{ cm}^{-2} \right)$, far away from the compressible boundary (Fig. 12). It is in sharp contrast to the $\nu = 1$ data at *high* n near the compressible boundary $\left(n > 10 \times 10^{10} \text{ cm}^{-2} \right)$, where R_{xx} *vs.* T^{-1} data appear to simply shift horizontally to *lower* T as n is *raised.*

While we do not have a clear understanding of this peculiar data, it is possible that a *finite-temperature* transition from a QHE to a compressible state is taking place, with T^* marking this transition. Although unprecedented in a single-layer 2DES, finite-T transitions may occur in bilayer systems with appropriate parameters: examples include the

Kosterlitz-Thouless transition theoretically proposed for the Ψ_{111}^1 state ([63,64], also see Steve Girvin's notes in this volume) or a transition from a correlated (Ψ_{111}^1-like) incompressible state to an uncorrelated, compressible state with $\nu = 1/2$ in each layer [67]. Details of such transitions and how they will quantitatively affect the transport properties are not known, however.

6.6 Spontaneous interlayer charge transfer

Another noteworthy feature of the data taken on this electron system is the appearance of FQH states at unusual fillings such as $\frac{11}{15}$ and $\frac{19}{15}$ which again have no counterparts in single-layer systems. The strongest of these occurs at $\nu = \frac{11}{15}$, between $\nu = \frac{2}{3}$ and $\frac{4}{5}$, and can be seen in Figure 22b as a dark blue strip for $\gamma \gtrsim 15$. We observe such states near the $\nu = \frac{2}{3}$ and $\frac{4}{3}$ FQH states as these become of 2C origin. Here we first present additional data on these states and then argue that they signal a spontaneous interlayer charge transfer at high magnetic fields [27].

Data of Figure 26, taken as the angle θ between the magnetic field and the normal to the 2D plane is varied, provide additional examples (see Fig. 15c for experimental geometry). Note that with increasing θ, for a given filling factor, the in-plane component of the magnetic field $(B_\parallel)$ increases and drives the system from 1C to 2C. This is because the in-plane magnetic field suppresses the tunneling and reduces Δ_{SAS} [68]. Data of Figure 26 reflect this expectation. The top trace of Figure 26a, taken at $\theta = 0$, shows essentially 1C FQH states while the lower trace which was taken at large θ exhibits predominantly 2C features: even-numerator FQH states at $\nu = \frac{2}{3}, \frac{4}{5}, \frac{4}{3}, \frac{6}{5}$, etc. The lower trace, however, reveals the presence of several other R_{xx} minima at unusual fillings between these even-numerator fillings, e.g., at $\nu = \frac{11}{15}, \frac{19}{15}$, and $\frac{29}{35}$.

Figure 26b summarizes the evolution of the FQH states in this electron system as a function of increasing θ. We have condensed a large set of traces onto the $(B_\perp, \theta)$ plane by mapping R_{xx} (normalized to its maximum value within the plotted parameter range) to a grayscale color between black and white. In such a plot, the IQHE and FQHE phases show up as dark black regions, whose width along the $B_\perp$ axis is a reflection of the strength of the associated state, i.e., the magnitude of its energy gap. The traces in Figure 26a can be interpreted as constant-θ slices through the image of Figure 26b. As θ is increased, the system is swept from the 1C through the 2C regime; a visible measure of this general evolution is the weakening and eventual collapse of the $\nu = 1$ QH state. The $\nu = \frac{3}{5}$ FQH state, another 1C state, is also destroyed by the increasing $B_\parallel$. For the states that can exist as both 1C and 2C phases, transitions between the two ground states are evident. For example, the $\nu = \frac{2}{3}$ and $\frac{4}{5}$ states undergo a 1C to 2C transition at $\theta \simeq 18°$ and $27°$, respectively. Nestled between these two states and in
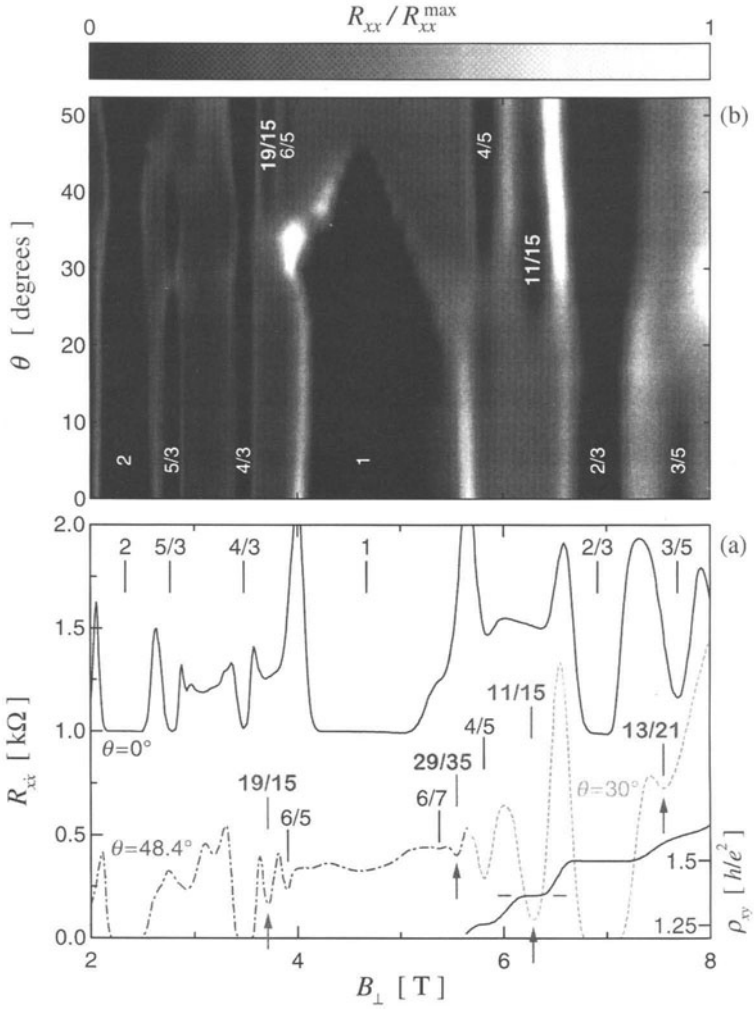
Fig. 26. Tuning the bilayer electron system (at fixed $n = 11.2 \times 10^{10}$ cm^{-2}) from the 1C to the 2C regime by increasing θ (hence $B_{\parallel}$) (a) R_{xx} vs. $B_{\perp}$ "slices" through the image of (b), where the normalized R_{xx} is mapped to a gray scale and also plotted vs. θ (total fillings ν are labeled). Spontaneous interlayer charge transfer engenders new FQH liquids (see features marked by vertical arrows and bold fractions). (After Manoharan *et al.* [27].)

close proximity to their 1C↔2C transitions, an $\frac{11}{15}$ FQH state develops and becomes quite strong. At the same time, ρ_{xy} exhibits a quantized plateau at $\frac{15}{11}\left(h/e^2\right)$ (see lower right of Fig. 26a). Very similar behavior is observed
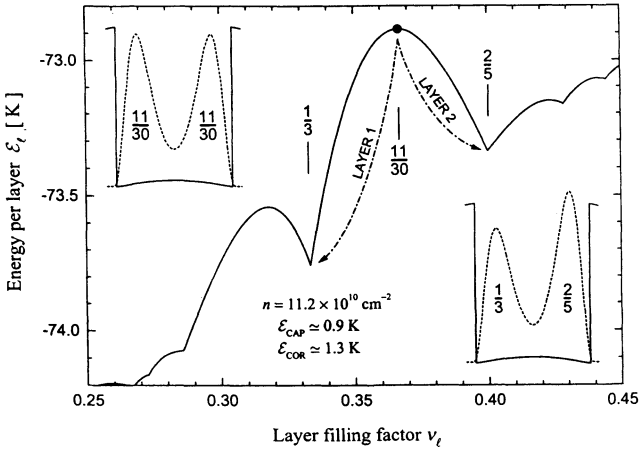
Fig. 27. Competition between capacitive charging energy ε_{CAP} (insets) and liquid correlation energy ε_{COR} (arrows) governing the susceptibility toward spontaneous interlayer charge transfer. Displayed fractions are layer fillings ν_ℓ. (After Manoharan *et al.* [27].)

on the other side of $\nu = 1$ in Figure 26b. A $\frac{19}{15}$ state develops in the vicinity of the $\nu = \frac{4}{3}$ 1C$\leftrightarrow$2C transition (at $\theta \simeq 35°$) along with the appearance of the 2C $\frac{6}{5}$ state (at $\theta \simeq 38°$).

What is the origin of these "special" states? We argue that at these fillings, interlayer charge transfer takes place so that two strong FQH states (at different layer fillings) stabilize in separate layers. The idea is best illustrated in Figure 27 (insets): the system at $\nu = \frac{11}{15}$ (layer filling $\frac{11}{30}$) deforms itself so that one layer locks in the strong $\frac{1}{3}$ FQH state and the other the $\frac{2}{5}$ state (note that $\frac{11}{15} = \frac{1}{3} + \frac{2}{5}$). What drives this "phase-separation" into two compressible FQH liquids is the presence of downward "cusps" in the ground state energy of the system at the magic FQHE fractions (Fig. 27). An estimate of the energy *savings* from such transfer is made in Figure 27 where the calculated ground states are plotted as a function of layer filling ν_ℓ. For details of how this calculation was made, see references [27] and [28]. The estimated correlation energy gained by forming the incompressible $\frac{1}{3}$ and $\frac{2}{5}$ FQH liquid states in the two separate layers, $\simeq 1.3$ K, is indeed quite comparable to the electrostatic (capacitive) energy cost, $\simeq Q^2/2nC \simeq 0.9$ K, for transferring the appropriate fraction $\left(\frac{1}{30}\right)$ of electrons from one layer to the other (Q is the transferred charge and C is the interlayer capacitance) [27]. The interlayer charge transfer interpretation therefore seems plausible.

The data presented so far show the presence of FQH states such as $\nu = \frac{11}{15}$ when the electron system is made 2C by either going to high density (Fig. 15a) or at large θ (Fig. 15c). In both these cases the electron system
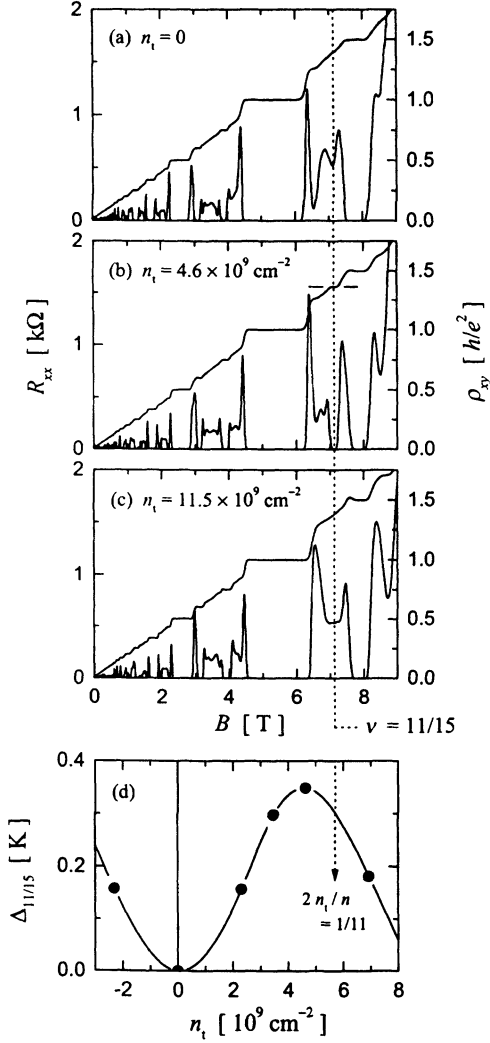
Fig. 28. Intentionally imposed interlayer charge transfer n_t will stabilize (b) an incompressible layered $\left(\frac{1}{3} + \frac{2}{5}\right)$ FQH state at $\nu = \frac{11}{15}$ when the charge distribution is imbalanced close to the expected $(5 : 6)$ layer density ratio [dotted line in (d)]. (After Manoharan et al. [27].)

has a *symmetric* (balanced) charge distribution at zero magnetic field, and we are conjecturing that at high $B_\perp$ the interlayer charge transfer takes place. To verify this conjecture, we did the following experimental test at $\theta = 0$. We start with the electron system at an n where the $\nu = \frac{2}{3}$ FQH

state has just become 2C so that the incompressible state at $\frac{11}{15}$ has barely developed (*e.g.*, $n = 12.6 \times 10^{10}$ cm^{-2}; see Fig. 28a). Now suppose we keep n fixed but intentionally *impose* an interlayer charge transfer n_t by applying a perpendicular *electric* field (physically generated *via* front- and back-gate biases of opposite sign, as schematically shown in Fig. 15b). As we transfer charge, the $\frac{11}{15}$ FQH state should get stronger as $2n_t/n$ approaches the ratio $\left(\frac{2}{5} - \frac{1}{3}\right) / \left(\frac{2}{5} + \frac{1}{3}\right) = \frac{1}{11}$, and then should become weaker once $2n_t/n$ exceeds $\frac{1}{11}$. The data shown in Figures 28a-c demonstrate that this behavior is indeed observed in our experiment. In particular, the quasiparticle excitation gap $\Delta_{11/15}$ measured for the $\frac{11}{15}$ FQH state is largest when the $2n_t/n$ exceeds $\frac{1}{11}$, *i.e.* layer densities imbalanced in the ratio $\left(\frac{1}{3} : \frac{2}{5}\right) = (5 : 6)$ (Fig. 28d).

Two additional features of the data in Figure 26 are noteworthy. First, the $\nu = \frac{11}{15}$ state appears to become weaker with increasing $\theta \gtrsim 40°$. This is reasonable and stems from the fact that spontaneous charge transfer will only occur if the correlation energy savings overcome the capacitive energy cost. At very large $B_{\parallel}$ (or n), the two layers become increasingly more isolated and the capacitive energy opposing charge transfer begins to dominate any correlation energy savings that would come from a $\left(\frac{1}{3} + \frac{2}{5}\right)$ state. Thus, the system remains compressible, as expected for two distant and weakly-coupled parallel 2DESs at $\nu = \frac{11}{15}$ $\left(\frac{11}{30}\right.$ filling in each layer). Second, the R_{xx} minimum near $\nu = \frac{29}{35}$ $\left(= \frac{2}{5} + \frac{3}{7}\right)$ suggests a developing FQH state at this filling (Fig. 26). Such a state can be stabilized if, at $\nu = \frac{29}{35}$, there is an interlayer charge transfer so that one layer supports a FQH state at $\frac{2}{5}$ filling and the other at $\frac{3}{7}$. Similarly, the weak R_{xx} minimum observed near $\nu = \frac{13}{21}$ (Fig. 26a) may hint at a developing FQH state stabilized by the formation of $\frac{1}{3}$ and $\frac{2}{7}$ FQH states in the separate layers.

6.7   Summary

Magnetotransport data taken on an electron system in a wide quantum well with variable density reveal a striking evolution of its correlated states. While the data at low and high densities are consistent with single-layer and weakly-coupled bilayer states respectively, at intermediate densities the data exhibit new QHE and insulating phases which are stabilized by both intralayer and *interlayer* electron correlations.

References

[1] von Klitzing K. , Dorda G. and Pepper M., *Phys. Rev. Lett.* **45** (1980) 494.

[2] Laughlin R.B., *Phys. Rev. B* **23** (1981) 5632.

[3] Tsui D.C., Stormer H.L. and Gossard A.C., *Phys. Rev. Lett.* **48** (1982) 1559.

[4] Laughlin R.B., *Phys. Rev. Lett.* **50** (1983) 1395.

[5] Many of the reports on the physics of 2D systems can be found in the proceedings of the international conferences on the *Electronic Properties of Two-dimensional Systems* (EP2DS), which are held every two years. For recent proceedings, see: *Surf. Sci.* **305** (1994); *Surf. Sci.* **361/362** (1996); *Physica B* **249-251** (1998).

[6] Prange R.E. and Girvin S.M., *The Quantum Hall Effect*, 2nd ed. (Springer-Verlag, New York, 1990).

[7] Chakraborty T. and Pietilainen P., *The Quantum Hall Effects: Fractional and Integral* (Springer-Verlag, Berlin 1995).

[8] Das S. Sarma and Pinczuk A., *Perspectives in Quantum Hall Effects* (Wiley, New York, 1997).

[9] MacDonald's A.H., Les Houches 1994 Notes, edited by E. Akkermans, G. Montambaux, J.-L. Pichard and J. Zinn-Justin, *Mesoscopic Quantum Physics* (Elsevier, Amsterdam, 1995) p. 659.

[10] Stormer H.L., Dingle R., Gossard A.C., Wiegmann W. and Sturge M.D., *Solid State Commun.* **29** (1979) 705.

[11] For a simple and useful text on semiconductor heterostructures, see J.H. Davies, *The Physics of Low-Dimensional Semiconductors* (Cambridge University Press Cambridge, 1998). Other useful books and review articles are: Bastard G., *Wave Mechanics Applied to Semiconductor Heterostructures* (Halsted Press, New York, 1988); Weisbuch C. and Vinter B., *Quantum Semiconductor Structures*, Academic Press, New York, 1991; M.J. Kelly, *Low-Dimensional Semiconductors, Materials, Physics, Technology, Devices* (Clarendon Press, Oxford, 1995).

[12] For a comprehensive review of the 2D physics in the pre-QHE era see Ando T., Fowler A.B. and Stern F., *Rev. Mod. Phys.* **54** (1982) 437.

[13] Cho A.Y., *Mater. Res. Soc. (MRS) Bull.* **20** (1995) 21.

[14] Etienne B. and Paris E., *J. Phys. France* **48** (1987) 2049.

[15] Shayegan M., Goldman V.J., Santos M., Sajoto T., Engel L. and Tsui D.C., *Appl. Phys. Lett.* **53** (1988) 2080.

[16] Shayegan M., Goldman V.G., Jiang C., Sajoto T. and Santos M., *Appl. Phys. Lett.* **52** (1988) 1086.

[17] Pfeiffer L.N., West K.W., Stormer H.L. and Baldwin K.W., *Appl. Phys. Lett.* **55** (1989) 1888.

[18] Sajoto T., Suen Y.W., Engel L.W., Santos M.B. and Shayegan M., *Phys. Rev. B* **41** (1990) 8449.

[19] Stern F., *Appl. Phys. Lett.* **43** (1983) 974; Gold A., *Phys. Rev. B* **44** (1991) 8818.

[20] Grimes C.C. and Adams G., *Phys. Rev. Lett.* **42** (1979) 795; for a review, see reference [12].

[21] For a review of recent developments in the magnetic-field-induced Wigner crystal states of 2D systems see articles by M. Shayegan (experiments) and H.A. Fertig (theory) in reference [8].

[22] Willett R.L., Stormer H.L., Tsui D.C., Gossard A.C. and English J.H., *Phys. Rev. B* **37** (1988) 8476.

[23] Shayegan M., Jo J., Suen Y.W., Santos M. and Goldman V.J., *Phys. Rev. Lett.* **65** (1990) 2916.

[24] He S., Zhang F.C., Xie X.C. and Das Sarma S., *Phys Rev. B* **42** (1990) 11376.

[25] de-Picciotto R., Reznikov M., Heiblum M., Umansky V., Bunin G. and Mahalu D., *Nature* **389** (1997) 162; Saminadayar L., Glattli D.C., Jin Y. and Etienne B., *Phys. Rev. Lett.* **79** (1997) 2526.

[26] For a review of composite Fermions and the FQHE, see theory articles by Jain J.K. and by Halperin B.I. in reference [8]. Also included in reference [8] is a comprehensive review, by Stormer H.L. and Tsui D.C., of the experimental results supporting the CF picture.

[27] Manoharan H.C., Suen Y.W., Lay T.S., Santos M.B. and Shayegan M., *Phys. Rev. Lett.* **79** (1997) 2722.

[28] Manoharan H.C., Ph.D. Thesis (Princeton University, 1998).

[29] Goldman V.J., Su B. and Jain J.K., *Phys. Rev. Lett.* **72** (1994) 2065.

[30] Shayegan M., *Solid State Commun.* **102** (1997) 155.

[31] Nicholas R.J., Haug R.J., K.v. Klitzing and Weimann G., *Phys. Rev. B* **37** (1988) 1294.

[32] Sondhi S.L., Karlhede A., Kivelson S.A. and Rezayi E.H., *Phys. Rev. B* **47** (1993) 16419.

[33] Skyrme T.H.R., *Proc. Soc R.. London, Ser. A* **247** (1958) 260.

[34] Moon K., Mori H., Kun Yang, Girvin S.M., MacDonald A.H., Zheng L., Yoshioka D. and Shou-Cheng Zhang, *Phys. Rev. B* **51** (1995) 5138.

[35] Barrett S.E., Dabbagh G., Pfeiffer L.N., West K. and Tycko R., *Phys. Rev. Lett.* **74** (1995) 5112.

[36] Brey L., Fertig H.A., Cote R. and MacDonald A.H., *Phys. Rev. Lett.* **75** (1995) 2562.

[37] Schmeller A., Eisenstein J.P., Pfeiffer L.N. and West K.W., *Phys. Rev. Lett.* **75** (1995) 4290.

[38] Aifer E.H., Goldberg B.B. and Broido D.A., *Phys. Rev. Lett.* **76** (1996) 680.

[39] Tycko R., Barrett S.E., Dabbagh G. and Pfeiffer L.N., *Science* **268** (1995) 1460.

[40] Bayot V., Grivei E., Santos M.B. and Shayegan M., *Phys. Rev. Lett.* **76** (1996) 4584.

[41] See, *e.g.* Wang J.K., Tsui D.C., Santos M.B. and Shayegan M., *Phys. Rev. B* **45** (1992) 4384.

[42] Bayot V., Grivei E., Beuken J.-M., Melinte S. and Shayegan M., *Phys. Rev. Lett.* **79** (1997) 1718.

[43] Côté R., MacDonald A.H., Brey L., Fertig H.A., Girvin S.M. and Stoof H.T.C., *Phys. Rev. Lett.* **78** (1997) 4825.

[44] Willett R., Eisenstein J.P., Stormer H.L., Tsui D.C., Gossard A.C. and English J.H., *Phys. Rev. Lett.* **59** (1987) 1776; Haldane F.D.M. and Rezayi E.H., *Phys. Rev. Lett.* **60** (1988) 956.

[45] Clark R.G., Haynes S.R., Suckling A.M., Mallett J.R., Wright P.A., Harris J.J. and Foxon C.T., *Phys. Rev. Lett.* **62** (1989) 1536; Eisenstein J.P., Stormer H.L., Pfeiffer L. and West K.W., *ibid* (1989) 1540.

[46] Suen Y.W., Jo J., Santos M., Engel L.W., Hwang S.W. and Shayegan M., *Phys. Rev. B* **44** (1991) 5947.

[47] Suen Y.W., Engel L.W., Santos M.B., Shayegan M. and Tsui D.C., *Phys. Rev. Lett.* **68** (1992) 1379.

[48] Suen Y.W., Santos M.B. and Shayegan M., *ibid* **69** (1992) 3551.

[49] Suen Y.W., Manoharan H.C., Ying X., Santos M.B. and Shayegan M., *Phys. Rev. Lett.* **72** (1994) 3405.

[50] Lay T.S., Suen Y.W., Manoharan H.C., Ying X., Santos M.B. and Shayegan M., *Phys. Rev. B* **50** (1994) 17725.

[51] Manoharan H.C., Suen Y.W., Santos M.B. and Shayegan M., *Phys. Rev. Lett.* **77** (1996) 1813.

[52] The $\nu = 1/2$ FQH state is also observed in bilayer electron systems in *double* quantum wells. [Eisenstein J.P., Boebinger G.S., Pfeiffer L.N., West K.W. and He S., *Phys. Rev. Lett.* **68** (1992) 1383].

[53] Halperin B.I., Helv. *Phys. Acta.* **56** (1983) 75.

[54] Yoshioka D., MacDonald A.H. and Girvin S.M., *Phys. Rev. B* **39** (1989) 1932.

[55] He S., Das Sarma S. and Xie X.C., *Phys. Rev. B* **47** (1993) 4394.

[56] MacDonald A.H., *Surf. Sci.* **229** (1990) 1.

[57] Suen Y.W., Ph.D. Thesis (Princeton University, 1994).

[58] Shahar D., Tsui D.C., Shayegan M., Bhatt R.N. and Cunningham J.E., *Phys. Rev. Lett.* **74** (1995) 4511.

[59] Oji H.C., MacDonald A.H. and Girvin S.M., *Phys. Rev. Lett.* **58** (1987) 824; L. Świerkowski, D. Neilson and J. Szymański, *Phys. Rev. Lett.* **67** (1991) 240.

[60] Price R., Zhu X., DasSarma S. and Platzman P.M., *Phys. Rev. B* **51** (1995) 2017.

[61] Zheng L. and Fertig H.A., *Phys. Rev. B* **52** (1995) 12282; Navasimhan S. and Ho T.-L., *Phys. Rev. B* **52** (1995) 12291.

[62] Chakraborty T. and Pietilainen P., *Phys. Rev. Lett. B* **59** (1987) 2784; Fertig H.A., *Phys. Rev. B* **40** (1989) 1087.

[63] Wen X.G. and Zee A., *Phys. Rev. Lett.* **69** (1992) 1811; Ezawa F. and Iwazaki A., *Int. J. Mod. Phys. B* **6** (1992) 3205.

[64] Moon K., Mori H., Yang K., Girvin S.M., MacDonald A.H., Zheng A.H., Yoshioka D. and Zhang S.C., *Phys. Rev. B* **51** (1995) 5138.

[65] Murphy S.Q., Eisenstein J.P., Boebinger G.S., Pfeiffer L.N. and West K.W., *Phys. Rev. Lett.* **72** (1994) 728.

[66] See, *e.g.*, Usher A., Nicholas R.J., Harris J.J. and Foxon C.T., *Phys. Rev. B* **41** (1990) 1129.

[67] Wen X.G. (private communication).

[68] Hu J. and MacDonald A.H., *Phys. Rev. B* **46** (1992) 12554.